

# Direct Evidence of Quasar Radiative and Mechanical Feedback in IRAS 09104+4109

K. W. Cavagnolo<sup>1\*</sup>, M. Donahue<sup>2</sup>, B. R. McNamara<sup>1,3,4</sup>, G. M. Voit<sup>2</sup>, and M. Sun<sup>5</sup>

<sup>1</sup>*Department of Physics and Astronomy, University of Waterloo, Waterloo, ON N2L 3G1, Canada.*

<sup>2</sup>*Department of Physics and Astronomy, Michigan State University, East Lansing, MI, 48824-2320, USA.*

<sup>3</sup>*Perimeter Institute for Theoretical Physics, 31 Caroline St. N., Waterloo, Ontario, N2L 2Y5, Canada*

<sup>4</sup>*Harvard-Smithsonian Center for Astrophysics, 60 Garden Street, Cambridge, MA 02138, USA*

<sup>5</sup>*Department of Astronomy, University of Virginia, Charlottesville, VA, 22904, USA.*

Accepted (2010 Month Day). Received (2010 Month Day); in original form (2010 Month Day)

## ABSTRACT

We present a detailed study of the hyperluminous infrared brightest cluster galaxy IRAS 09104+4109 using a deep *Chandra* X-ray observation.

**Key words:** cooling flows – galaxies: clusters: galaxies: individual (IRAS 09104+4109): clusters: individual (RX J0913.7+4056)

## 1 INTRODUCTION

IRAS 09104+4109 (hereafter, IRAS09) is an uncommon low-redshift ( $z = 0.4418$ ) ultraluminous infrared galaxy (ULIRG;  $L_{\text{IR}} > 10^{12} L_{\odot}$ ). Unlike most ULIRGs, IRAS09 is the brightest cluster galaxy (BCG) in a rich galaxy cluster, but unlike most BCGs, IRAS09 is a Seyfert-2 with 99% of the bolometric luminosity emerging longward of  $1 \mu\text{m}$  due to a heavily-obscured quasar (QSO) with a luminosity  $\sim 10^{47} \text{ erg s}^{-1}$  (Kleinmann et al. 1988; Hines & Wills 1993; Fabian et al. 1994; Evans et al. 1998; Franceschini et al. 2000; Iwasawa et al. 2001).

Data reduction is discussed in Section 2. Properties of the ICM are analyzed in Sections 3 and 4. Analysis of the ICM cavities, SMBH fueling, and QSO irradiation of the ICM are given in Sections 5, 6, and 7, respectively. The complex nuclear source is discussed in Section 8. Interpretation of the results is given in Section 9, with a brief summary in Section 10. A  $\Lambda$ CDM cosmology with  $H_0 = 70 \text{ km s}^{-1} \text{ Mpc}^{-1}$ ,  $\Omega_{\text{M}} = 0.27$ , and  $\Omega_{\Lambda} = 0.73$  is adopted, for which a redshift of  $z = 0.4418$  corresponds to  $\approx 9.1 \text{ Gyr}$  for the age of the Universe,  $D_A \approx 5.72 \text{ kpc arcsec}^{-1}$ , and  $D_L \approx 2.45 \text{ Gpc}$ .

## 2 OBSERVATIONS AND DATA REDUCTION

Unless stated otherwise, all spectral fits were performed over the energy range 0.7–7.0 keV with the  $\chi^2$  statistic in XSPEC 12.4 (Arnaud 1996) using an absorbed, single-temperature MEKAL model (Mewe et al. 1985) with abundance as a free parameter (Anders & Grevesse 1989 distribution) and quoted uncertainties of 90% confidence. All spectral models had the Galactic absorbing column density fixed at  $N_{\text{H,Gal}} = 1.58 \times 10^{20} \text{ cm}^{-2}$  (Kalberla et al. 2005). For the ICM, we assumed a mean molecular weight of  $\mu = 0.597$  and adiabatic index  $\gamma = 5/3$ .

### 2.1 *Chandra*

A 77.2 ks observation of IRAS09 was taken on 2009 January 09 with the ACIS-I instrument (ObsID 10445; PI Cavagnolo). The 9 ks archival *Chandra* observation of IRAS09 from 1999 November 03 taken with the ACIS-S array was included in our analysis (ObsID 509; PI Fabian). Both datasets were reprocessed and reduced using CIAO and CALDB versions 4.2. X-ray events were selected using ASCA grades, and corrections for the ACIS gain change, charge transfer inefficiency, and degraded quantum efficiency were applied. Point sources were located and excluded using WAVDETECT and visual inspection. Light curves from a source free region of each observation were created for a front-illuminated and back-illuminated CCD and compared to look for flares. Time intervals which fell outside 20% of the mean background count rate were excluded. After flare exclusion, the final exposure times for ObsID 509 and 10445 were 7 ks and 76 ks, respectively.

For imaging analysis, the flare-clean events files were reprojected to a common tangent point and summed. The astrometry of the ObsID 509 dataset was improved using a new aspect solution created with the CIAO tool REPROJECT\_ASPECT and the positions of several field sources. After astrometry correction, the positional accuracy between both observations was comparable to the resolution limit of the ACIS detectors. We refer to the final point source free, flare-clean, exposure-corrected images as the “clean” images. In Figure 1 are the 0.5–10.0 keV mosaiced clean image of RX J0913.7+4056, a zoom-in of the core region harboring IRAS09, and photons in the energy range 4.35–4.50 keV associated with the Fe K $\alpha$  fluorescence line from the nucleus (discussed in Section 8). Unless stated otherwise, the X-ray analysis in this paper relates to the *Chandra* data only.

\* Email: kcavagno@uwaterloo.ca

## 2.2 XMM-Newton

XMM-Newton data is utilized in Section 8 to check our results for the nuclear source against the analysis presented in Piconcelli et al. (2007). XMM-Newton observed IRAS09 on 2003 April 23 for 14 ks with the EPIC PN and MOS detectors (ObsID 0147671001; PI Fiore). Data was reprocessed using SAS version 7.1 and CCF release 258. Events files were created using the tools EMCHAIN and EPCHAIN for patterns 0-4. Light curves were extracted from the energy range 10-12 keV for the full field after cluster emission and Chandra identified point sources were removed. After flare exclusion, the effective exposure times for PN and MOS were 10 ks and 12 ks, respectively. A source spectrum grouped to 20 counts per energy channel was extracted from a region centered on the X-ray peak and extending to  $R_{500}$  (defined in Section 3). A background spectrum was extracted from a source-free region with an area equal to the source region.

## 2.3 BeppoSAX

Conclusions reached in previous studies regarding the nature of the IRAS09 nuclear absorber have relied on the BeppoSAX hard X-ray detection discussed by Franceschini et al. (2000). Here, we repeat and confirm that analysis in order to compare our results in Section 8 against Franceschini et al. (2000). We retrieved and re-analyzed the BeppoSAX data taken 1998 April 18 (ObsCode 50273002; PI Franceschini). The data was reduced and analyzed with SAXDAS version 2.3.1 using the calibration data, cookbook, and epoch appropriate response functions available from HEASARC<sup>1</sup>.

Data from the PDS instrument ( $E_{\text{sens}} = 15\text{--}300$  keV) was accumulated, screened for good time intervals, and then a light curve was extracted. No significant variations of the light curve were detected. A PDS total spectrum was extracted from the on-axis data, and background subtraction was performed using the variable rise time threshold. Using data from the LECS ( $E_{\text{sens}} = 0.1\text{--}10$  keV) and MECS ( $E_{\text{sens}} = 1\text{--}10$  keV) instruments, spectra were extracted from the region enclosed by  $R_{500}$  with a background spectrum taken from an annulus outside  $R_{500}$ . We measure a PDS 15-80 keV count rate of  $0.106 \pm 0.055$  ct s<sup>-1</sup>. Fitting the PDS spectrum over the energy range 20-200 keV with an absorbed power-law having fixed spectral index of  $\Gamma = 1.7$  yielded fluxes of  $f_{10\text{--}200} = 2.09^{+1.95}_{-1.95} \times 10^{-11}$  erg s<sup>-1</sup> cm<sup>-2</sup> and  $f_{20\text{--}100} = 1.10^{+1.57}_{-1.63} \times 10^{-11}$  erg s<sup>-1</sup> cm<sup>-2</sup>. The count rate and fluxes are consistent with the results presented in Franceschini et al. (2000).

## 2.4 INTEGRAL & Swift

In this section we show that INTEGRAL and Swift data do not reveal any hard X-ray sources in the vicinity of IRAS09, but that the flux upper limits are consistent with the BeppoSAX PDS detection. Assuming the upper limits are representative of an  $\approx 1^\circ$  region around IRAS09 (i.e. the full-width half maximum PDS field of view), the lack of detected hard X-ray sources near IRAS09 suggests that the PDS detection did not originate from a brighter off-axis source, assuming the source is/was not transient or a one-off event.

Between 2005–2007, IRAS09 was within the INTEGRAL field of view during 85 pointings. Data was collected with the ISGRI

( $E_{\text{sens}} = 15\text{ keV--}1\text{ MeV}$ ) and JEM-X ( $E_{\text{sens}} = 3\text{--}35\text{ keV}$ ) instruments for 81 and 79 pointings, respectively. Datasets were reduced using OSA version 8.0 and version 8.0.1 of the Instrument Characteristics. For each instrument, mosaiced images of intensity, significance, variance, and exposure were generated from the background-subtracted images of each pointing. The combined ISGRI and JEM-X effective exposure times were 200 ks and 210 ks, respectively. Versions 1 and 30 of the INTEGRAL Reference Catalogue were used for source detection. The OSA source detection routines did not locate any  $5\sigma$  sources in the ISGRI and JEM-X mosaiced images. Additional visual inspection of the images did not reveal any features which might suggest emission from a source.

The ISGRI and JEM-X instrument responses have a strong energy dependence, thus, upper limits calculated using only the variance images (i.e. assuming uniform sensitivity) will systematically underestimate the flux limit. To account for this variation, flux upper limits were derived by integrating the ISGRI and JEM-X responses over a specified energy range and weighting by an assumed spectral shape. We assumed the IRAS09  $E > 10$  keV spectrum goes as  $S_\nu = \nu^{-1.7}$  with no high-energy cut-off. Between 10-35 keV and 20-100 keV, we derive  $3\sigma$  upper limits of  $f_{10\text{--}35} = 1.28 \times 10^{-12}$  erg s<sup>-1</sup> cm<sup>-2</sup> and  $f_{20\text{--}100} = 5.70 \times 10^{-11}$  erg s<sup>-1</sup> cm<sup>-2</sup>, respectively. The INTEGRAL  $1\sigma$  20-100 keV flux limit is narrowly higher than the BeppoSAX 20-100 keV PDS measured flux, and is consistent with a  $z = 0.44$  source which would not be detected in the IBIS Extragalactic AGN Survey (Bassani et al. 2006). As a check of our analysis, the 22 month Swift-BAT ( $E_{\text{sens}} = 15\text{--}150$  keV) survey (Tueller et al. 2010) was searched for sources within  $5^\circ$  of IRAS09. The survey has a 14-195 keV  $4.8\sigma$  detection limit of  $2.2 \times 10^{-11}$  erg s<sup>-1</sup> cm<sup>-2</sup>, 14% higher than the 14-195 keV IRAS09 flux expected based on the BeppoSAX detection, and consistent with the INTEGRAL upper limits, no sources were found.

## 2.5 VLA

From 1986 to 2000, IRAS09 was observed with VLA at multiple radio frequencies and resolutions. Hines & Wills (1993, hereafter H93) also present analysis of 1.4 and 5 GHz VLA observations. Continuum mode observations were taken from the VLA archive and reduced using version 3.0 of the Common Astronomy Software Applications (CASA). Flagging of bad data was performed using a combination of CASA's FLAGDATA tool in RFI mode and manual inspection. Radio images were generated by Fourier transforming, cleaning, self-calibrating, and restoring individual radio observations. The additional steps of phase and amplitude self-calibration were included to increase the dynamic range and sensitivity of the radio maps. All sources within the primary beam and first side-lobe detected with fluxes  $> 5\sigma_{\text{rms}}$  were imaged to further maximize the sensitivity of the radio maps.

Resolved radio emission associated with IRAS09 is detected at 1.4 GHz, 5.0 GHz, and 8.4 GHz, while a  $3\sigma$  upper limit of 0.84 mJy is established at 14.9 GHz. Fluxes for unresolved emission at 74 MHz, 151 MHz, and 325 MHz were retrieved from VLSS (Cohen et al. 2007), 7C Survey (Riley et al. 1999), and WENSS (Rengelink et al. 1997), respectively. No formal detection is found in VLSS, however, an overdensity of emission at the location of IRAS09 is evident. For completeness, we measured a flux for the potential source, but excluded the value during fitting of the radio spectrum.

The combined 1.4 GHz image reveals the most extended structure, and thus our discussion regarding radio morphology is guided

<sup>1</sup> <http://heasarc.nasa.gov/docs/sax>

using this frequency. The deconvolved, integrated 1.4 GHz flux of the continuous extended structure coincident with IRAS09, and having  $S_V \gtrsim 3\sigma_{\text{rms}}$ , is  $14.0 \pm 0.51$  mJy. A significant spur of radio emission northeast of the nucleus is detected with flux  $0.21 \pm 0.07$  mJy. Radio contours were generated beginning at 3 times the rms noise and moving up in 6 log-space steps to the peak intensity of  $4.7 \text{ mJy beam}^{-1}$ . These are the contours referenced in all following discussion of the radio source morphology and its interaction with the X-ray gas.

Below we determine properties of the radio source for the purpose of constraining the AGN outflow properties which created X-ray cavities in the RX J0913.7+4056 halo (see Section 5). The radio spectrum was fitted between 151 MHz and 8.4 GHz for the full radio source (lobes, jets, & core) with the well-known KP (Kardashev 1962; Pacholczyk 1970), JP (Jaffe & Perola 1973), and CI (Heavens & Meisenheimer 1987) synchrotron models. The models primarily vary in their assumptions regarding the electron pitch-angle distribution and number of injections. The models were fitted to the radio spectrum using the code of Waters & Zepf (2005), which is based on the method of Carilli et al. (1991). The JP model (single electron injection, randomized but isotropic pitch-angle distribution) yields the best fit with  $\chi^2(\text{DOF}) = 0.491(3)$ , a break frequency of  $\nu_B = 12.9 \pm 1.0$  GHz, and a low-frequency ( $\nu < 2$  GHz) spectral index of  $\alpha = -1.10 \pm 0.09$ . The bolometric radio luminosity was approximated by integrating under the JP curve between  $\nu_1 = 10$  MHz and  $\nu_2 = 10,000$  MHz, giving  $L_{\text{radio}} = 1.09 \times 10^{42} \text{ erg s}^{-1}$ . The radio spectrum and best-fit models are shown in Figure 2.

Assuming inverse-Compton (IC) scattering and synchrotron emission are the dominant radiative mechanisms of the radio source, the time since acceleration for an isotropic particle population is given by Slee et al. (2001) as

$$t_{\text{sync}} = 1590 \left( \frac{B^{1/2}}{B^2 + B_{\text{CMB}}^2} \right) [\nu_B(1+z)]^{-1/2} \text{ Myr} \quad (1)$$

where  $B$  [ $\mu\text{G}$ ] is magnetic field strength,  $B_{\text{CMB}} = 3.25(1+z)^2$  [ $\mu\text{G}$ ] is a correction for IC losses to the cosmic microwave background,  $\nu_B$  [GHz] is the radio spectrum break frequency, and  $z$  is the dimensionless source redshift. Note that this form for  $t_{\text{sync}}$  neglects energy lost to adiabatic expansion of the radio plasma (Scheuer & Williams 1968). We assume that  $B$  is not significantly different from the equipartition magnetic field strength,  $B_{\text{eq}}$ , which is derived from the minimum energy density condition as (Miley 1980)

$$B_{\text{eq}} = \left[ \frac{6\pi c_{12}(\alpha, \nu_1, \nu_2) L_{\text{radio}} (1+k)}{V\Phi} \right]^{2/7} \mu\text{G} \quad (2)$$

where  $c_{12}(\alpha, \nu_1, \nu_2)$  is a dimensionless constant derived in Pacholczyk (1970),  $L_{\text{radio}}$  [ $\text{erg s}^{-1}$ ] is the integrated radio luminosity from  $\nu_1$  to  $\nu_2$ ,  $k$  is the dimensionless ratio of lobe energy in non-radiating particles to that in relativistic electrons,  $V$  [ $\text{cm}^3$ ] is the radio source volume, and  $\Phi$  is a dimensionless radiating population volume filling factor. Synchrotron age as a function of  $k$  and  $\Phi$  for the full radio source is shown in Figure 2. For various combinations of  $k$  and  $\Phi$ ,  $B_{\text{eq}} \approx 4\text{--}57 \mu\text{G}$ , with associated synchrotron ages in the range  $\approx 1\text{--}12$  Myr. Repeating the above analysis using only radio lobe emission at 1.4 GHz, 5.0 GHz, and an 8.4 GHz upper limit, reveals  $t_{\text{sync}}$  could be as high as 30 Myr as a result of a significantly steeper spectral index and lower break frequency.

### 3 GLOBAL ICM PROPERTIES

Our analysis begins at the cluster scale with the integrated properties of the RX J0913.7+4056 ICM hosting IRAS09. We define the mean cluster temperature,  $T_{\text{cl}}$ , as the ICM temperature within a core-excised aperture extending to  $R_{\Delta_c}$ , the radius at which the average cluster density is  $\Delta_c$  times the critical density for a spatially flat Universe. We chose  $\Delta_c = 500$  and used the relations from Arnaud et al. (2002) to calculate  $R_{\Delta_c}$ . RX J0913.7+4056 has a luminous, cool core and complex nucleus which are not representative of  $T_{\text{cl}}$ , thus, the convention of Maughan (2007) was followed and emission inside  $0.15 R_{500}$  was excised. Source spectra were extracted from the region  $0.15\text{--}1.0 R_{500}$  and background spectra were extracted from reprocessed CALDB blank-sky backgrounds (see Section 4). Because  $T_{\text{cl}}$  and  $R_{\Delta_c}$  are correlated in the adopted definitions, they were recursively determined until three consecutive iterations produced  $T_{\text{cl}}$  values which agreed within the 68% confidence intervals. We measure  $T_{\text{cl}} = 7.54^{+1.76}_{-1.15} \text{ keV}$  corresponding to  $R_{500} = 1.16^{+0.27}_{-0.19} \text{ Mpc}$ . Measurements for a variety of  $R_{\Delta_c}$  apertures are summarized in Table 1. The BCG nucleus emits strong Fe K $\alpha$  emission which affects the spectral fitting, and for any aperture including the core, the nucleus was excluded using a region twice the size of the *Chandra* PSF 90% EEF (see Section 8 for details).

The cluster gas and gravitational masses were derived using the deprojected radial electron density and temperature profiles presented in Section 4. Electron gas density,  $n_e$ , was converted to total gas density as  $n_g = 1.92 n_e \mu m_{\text{H}}$  where  $m_{\text{H}}$  [g] is the mass of hydrogen. The gas density profile was fitted with a  $\beta$ -model (Cavaliere & Fusco-Femiano 1978), and the temperature profile was fitted with the 3D- $T(r)$  model of Vikhlinin et al. (2006) to ensure continuity and smoothness of the radial log-space derivatives when solving the hydrostatic equilibrium equation. Total gas mass was calculated by assuming spherical symmetry and integrating the best-fit  $\beta$ -model out to  $R_{200}$ , giving  $M_{\text{gas}}(r < R_{200}) = 7.99 (\pm 0.65) \times 10^{13} M_{\odot}$ . The gravitating mass was derived by solving the hydrostatic equilibrium equation using the analytic density and temperature profiles. We calculate  $M_{\text{grav}}(r < R_{200}) = 7.22 (\pm 1.44) \times 10^{14} M_{\odot}$ , giving a ratio of gas mass to gravitating mass of  $0.11 \pm 0.02$ . The gas and gravitating mass errors were estimated from 10,000 Monte Carlo realizations of the measured density and temperature profiles and their associated uncertainties.

In terms of the galaxy cluster population, RX J0913.7+4056 resides toward the high-end of the mass distribution with a luminosity-temperature ratio and gas fraction consistent with flux-limited and representative cluster samples (Reiprich & Böhringer 2002; Pratt et al. 2009). Adjusted for differences in assumed cosmology, our global measurements agree with prior studies of IRAS09 (*e.g.* Allen 2000). With the exception of the strange BCG at its heart, RX J0913.7+4056 appears to be a typical massive, relaxed galaxy cluster. None of the integrated X-ray cluster properties suggest the system has undergone a recent major merger or cluster-scale AGN outburst which may have dramatically disrupted the ICM. The lack of a detected radio halo also suggests no recent merger activity, previous powerful AGN outbursts, and possibly no turbulent motions in the core (*e.g.* Ferrari et al. 2008).

### 4 RADIAL ICM PROPERTIES

Now we discuss the finer global structure of RX J0913.7+4056 via radial ICM properties. Consistent with the analysis of Section 3, the



BCG nucleus was excluded from all radial analysis. Temperature ( $kT_X$ ) and abundance ( $Z$ ) profiles were created using circular annuli centered on the cluster X-ray peak and containing 2.5K and 5K source counts per annulus, respectively. A deprojected temperature profile was generated using the DEPROJ method in XSPEC. We use the projected profile in all analysis as it does not significantly differ from the deprojected profile. Spectra were grouped to 25 source counts per energy channel. CALDB blank-sky backgrounds were reprocessed and reprojected to match each observation, and then normalized for variations of the hard-particle background using the ratio of blank-sky and observation 9.5-12 keV count rates. Following the method outlined in Vikhlinin et al. (2005), a fixed background component was included during spectral analysis to account for the spatially-varying Galactic foreground (see Cavagnolo et al. 2008b, for more detail). The temperature and abundance profiles are shown in the top row of Figure 3. After masking out all X-ray substructure (see Section 7) and the central  $2''$ , a grouped spectrum for the central 20 kpc was fitted with a thermal model plus a cooling flow component. The best-fit model had a mass deposition rate of  $\dot{M} = 206^{+87}_{-65} M_\odot$  for upper and lower temperatures of 5.43 keV and 0.65 keV, respectively, with abundance  $0.51 Z_\odot$ .

A surface brightness (SB) profile was extracted using concentric  $1''$  wide circular annuli centered on the cluster X-ray peak. From the SB and temperature profiles, a deprojected electron density ( $n_e$ ) profile was derived using the Kriss et al. (1983) technique (see Cavagnolo et al. 2009, for more detail). Errors for the density profile were estimated from 10,000 Monte Carlo bootstrap resamplings of the SB profile. The SB and electron gas density profiles are shown in the second row of Figure 3.

Total gas pressure ( $P = 2.4kT_X n_e$ ), entropy ( $K = kT_X n_e^{-2/3}$ ), cooling time ( $t_{\text{cool}} = 3nkT_X [2n_e n_H \Lambda(T, Z)]^{-1}$ ), and enclosed X-ray luminosity ( $L_X$ ) profiles were also created. These profiles are presented in the bottom two rows of Figure 3. Uncertainties for each profile were calculated by propagating the individual parameter errors and then summing in quadrature. The cooling functions,  $\Lambda(T, Z)$ , used to calculate cooling times were derived from the best-fit spectral model for each annulus of the temperature profile and interpolated onto the grid of the higher resolution density profile. The function  $K(r) = K_0 + K_{100}(r/100 \text{ kpc})^\alpha$  was fitted to the entropy profile, giving best-fit values of  $K_0 = 12.6 \pm 2.9 \text{ keV cm}^2$ ,  $K_{100} = 139 \pm 8 \text{ keV cm}^2$ , and  $\alpha = 1.71 \pm 0.10$ .

The RX J0913.7+4056 ICM structure is typical of the cool core class of galaxy clusters, with a temperature profile that rises with increasing radius and an entropy profile with a relatively small, flattened core. There are no resolved discontinuities in the  $kT_X$ ,  $n_e$ , or  $P$  profiles to suggest the presence of a shock or cold front. Additional 2D analysis using the weighted Voronoi tessellation and contour binning methods of Diehl & Statler (2006) and Sanders (2006), respectively, also did not reveal any significant temperature or abundance substructure. The entropy profile is consistent with the cool core population as a whole (Cavagnolo et al. 2009), and, in particular, with the population of  $K_0 < 30 \text{ keV cm}^2$  clusters that have radio-loud AGN and star formation in the BCG (Cavagnolo et al. 2008a; Rafferty et al. 2008). The  $K_0 \lesssim 30 \text{ keV cm}^2$  scale also defines an entropy regime in which thermal electron conduction in cluster cores is too inefficient to suppress widespread environmental cooling (Voit et al. 2008). Therefore, cooling subsystems, like gas ram pressure stripped from cluster members or ICM thermal instabilities, should be long-lived. There is an abundance of cool, gaseous substructure surrounding

IRAS09, and in Section 7 we discuss the relation of this structure to the AGN and QSO.

## 5 ICM CAVITY SYSTEM

To aid investigation of ICM substructure, a residual X-ray image was created by subtracting a SB model for the ICM from the mosaiced *Chandra* clean image. The *Chandra* clean image was binned by a factor of 2 and the SB isophotes were fitted using the IRAF tool ELLIPSE. The geometric parameters ellipticity ( $\epsilon$ ), position angle ( $\phi$ ), and centroid ( $C$ ) were initially free to vary, but the best-fit values for each isophote converged to mean values of  $\epsilon = 0.14$ ,  $\phi = -76^\circ$ , and  $C$  [J2000] = (09:13:45.5; +40:56:28.4). These values were fixed in the fitting routine to eliminate the isophotal twisting resulting from statistical variation of the best-fit values for each radial step. A SB model was constructed from the best-fit model and subtracted from the clean image. The resulting residual image is shown in Figure 4.

The faint SB decrements NW and SE of the nucleus in the clean image are resolved into cylindrical voids in the residual image. The void and radio jet morphologies closely trace each other, confirming they share a common origin in the AGN outburst. Cavities are a well-known phenomenon, but currently, IRAS09 is the highest redshift object where cavities have been directly imaged. In addition, IRAS09 is thus far the only example of a QSO-dominated system with an unambiguous cavity detection. Using a 1994 *ROSAT* HRI observation, Fabian & Crawford (1995) found a “hole” in the core of RX J0913.7+4056 which they attributed to absorption by a  $> 1000 M_\odot \text{ yr}^{-1}$  cooling flow. When juxtaposed with the *Chandra* residual image, the “hole” is clearly not associated with the real cavities, which are not resolved in the 1994 HRI. Neither the cavities nor the “hole” are seen in a longer 1995 HRI follow-up observation.

The AGN outburst energetics were investigated using properties of the cavities (see McNamara & Nulsen 2007, for a review). Cavity volumes,  $V$ , were calculated by approximating each void in the X-ray image with a right circular cylinder projected onto the plane of the sky along the cylinder radial axis. The lengthwise axis of the cylinders were assumed to lie in a plane perpendicular to the line of sight that passes through the central AGN. The energy in each cavity,  $E_{\text{cav}} = \gamma PV / (\gamma - 1)$ , was estimated by assuming the contents are a relativistic plasma ( $\gamma = 4/3$ ), and then integrating the total gas pressure,  $P$ , over the surface of each cylinder. The radio source morphology, spectrum, and age suggest the jets were recently, or still are, being fed by the central AGN. Thus, we assumed the cavities were created on a timescale dictated by the ambient gas sound speed,  $t_{\text{sonic}}$  (see Bîrzan et al. 2004), and the distance the AGN outflow has traveled to create each cavity was set to the cylinder length, not the midpoints, as is common. The power of each cavity is thus  $P_{\text{cav}} = E_{\text{cav}} / t_{\text{sonic}}$ . Cavity power is often assumed to be a good estimate of the physical quantity jet power,  $P_{\text{jet}}$ , but note that neither accounts for energy which may be imparted to shocks. Properties of the individual cavities are listed in Table 2.

The total cavity energy and power are estimated at  $E_{\text{cav}} = 5.11 (\pm 1.33) \times 10^{59} \text{ erg}$  and  $P_{\text{cav}} = 3.05 (\pm 1.03) \times 10^{44} \text{ erg s}^{-1}$ , respectively, with a mean  $P_{\text{cav}} = 1.52 (\pm 0.11) \times 10^{44} \text{ erg s}^{-1}$ . Radio power has been shown to be a reasonable surrogate for estimating mean jet power (Bîrzan et al. 2008). Thus, we checked the  $P_{\text{cav}}$  calculation using the Cavagnolo et al. (in preparation)  $P_{\text{jet}}-P_{\text{radio}}$  1.4 GHz and 200-400 MHz scaling relations. The relations give  $P_{\text{jet}} \approx 2-6 \times 10^{44} \text{ erg s}^{-1}$ , in agreement with the X-ray measure-

ments. Compared with other systems hosting cavities, IRAS09 resides between the middle and upper-end of the cavity power distribution. The AGN outburst is powerful, but there is nothing unusual about the energetics or the radiative efficiency ( $P_{\text{radio}}/P_{\text{jet}}$ ) given the cluster mass and ICM properties.

Of interest is how the AGN energetics compare to the cooling rate of the host X-ray halo. The cooling radius was set at the radius where the ICM cooling time is equal to  $H_0^{-1}$  at the redshift of IRAS09. We calculate  $R_{\text{cool}} = 128$  kpc, and measure an unabsorbed bolometric luminosity within this radius of  $L_{\text{cool}} = 1.61^{+0.25}_{-0.20} \times 10^{45}$  erg s $^{-1}$ . If all of the cavity energy is thermalized over  $4\pi$  sr, then  $\approx 20\%$  of the energy radiated away by gas within  $R_{\text{cool}}$  is replaced by energy coming from the AGN. Assuming the mean ICM cooling rate does not vary significantly on a timescale of  $\sim 1$  Gyr, this highly optimistic scenario implies that 5 similar power AGN outbursts will significantly suppress cooling of the cluster halo.

Our calculations neglect the influence of shocks, but the synchrotron age and cavity age are useful in addressing this issue. If  $t_{\text{sync}}$  is an accurate measure of the radio source age, then the age discrepancy  $t_{\text{sonic}} \gtrsim 42$  Myr versus  $t_{\text{sync}} \lesssim 30$  Myr implies the AGN outflow is supersonic, otherwise the radio-loud plasma will radiate away all its energy and be radio-silent prior to reaching the end of the observed jet. The implication being that some amount of energy may have gone into gas shocking. Recall, however, that no shocks are detected in the X-ray analysis, and note that the properties of IRAS09 nebulae are inconsistent with excitation due to shocks (Crawford & Vnderriest 1996; Tran et al. 2000). But, the nebular regions studied are  $\gtrsim 20$  kpc from the jet axis, and may not be indicative of gas dynamics close to the outflow. Regardless, the energy in shocks was crudely estimated by setting  $t_{\text{sonic}} = 20$  Myr and adjusting  $P_{\text{cav}}$  by the Mach number:  $\Delta P_{\text{cav}} = \Delta P / \Delta t$  and  $\Delta P \propto M^3$ . Relative to the ICM sound speed, the velocity needed to reach the end of the radio jet in 20 Myrs requires a Mach number of  $M \approx 2.5$ , which brings the outburst power up to  $\approx 1 \times 10^{46}$  erg s $^{-1}$  ( $E_{\text{cav}} \sim 10^{61}$  erg for a 20 Myr duration). Within the formal uncertainties, the AGN outburst power is on the order of a few times  $10^{44}$  erg s $^{-1}$ , with the possibility of being as large as  $10^{46}$  erg s $^{-1}$ .

## 6 FUELING THE AGN OUTBURST

An estimate of black hole mass,  $M_{\text{BH}}$ , is key to investigating what powers an AGN outburst. There are a variety of  $M_{\text{BH}}$  estimators, many of which rely on infrared or optical emission line measurements. The integrated IR and emission line properties of IRAS09, however, are dominated by hot dust and complex nebulae, and may not be representative of  $M_{\text{BH}}$ . Therefore,  $M_{\text{BH}}$  was constrained using a variety of relations and the weighted mean was used in subsequent calculations. Using a stellar velocity dispersion of  $\sigma_s = 293 \pm 6$  km s $^{-1}$ , determined from the Faber & Jackson (1976) relation and the corrected  $B$ -band magnitude from HyperLeda (Paturel et al. 2003), the Tremaine et al. (2002) relation gives  $M_{\text{BH}} = 0.63 (\pm 0.05) \times 10^9 M_{\odot}$ . The Graham (2007) relations relating absolute  $[B, R, K]$ -band magnitudes to  $M_{\text{BH}}$  predict  $M_{\text{BH}} = 0.5\text{--}5.0 \times 10^9 M_{\odot}$ . The weighted mean  $M_{\text{BH}}$  value we adopt is  $1.05 (\pm 0.17) \times 10^9 M_{\odot}$ .

Some of the gravitational binding energy of the material accreting onto the SMBH is transported outward via relativistic jets. Assuming this conversion has an efficiency  $\epsilon$ , the energy deposited in cavities by the jets implies an accretion mass expressed as  $\dot{M}_{\text{acc}} = E_{\text{cav}}/(\epsilon c^2)$  with a time-averaged mass accretion rate of

$\dot{M}_{\text{acc}} = M_{\text{acc}}/t_{\text{sonic}}$ . Setting  $\epsilon = 0.1$ , the AGN outburst resulted from the accretion of  $2.86 (\pm 0.75) \times 10^6 M_{\odot}$  of matter at a rate of  $0.054 \pm 0.004 M_{\odot} \text{ yr}^{-1}$ . If the accretion flow feeding the SMBH is spherically symmetric, it can be characterized in terms of the Eddington (Eqn. 3) and Bondi (Eqn. 4) accretion rates,

$$\dot{M}_{\text{Edd}} = \frac{2.2}{\epsilon} \left( \frac{M_{\text{BH}}}{10^9 M_{\odot}} \right) M_{\odot} \text{ yr}^{-1} \quad (3)$$

$$\dot{M}_{\text{Bon}} = 0.013 K_{\text{Bon}}^{-3/2} \left( \frac{M_{\text{BH}}}{10^9 M_{\odot}} \right)^2 M_{\odot} \text{ yr}^{-1} \quad (4)$$

where  $K_{\text{Bon}}$  [keV cm $^2$ ] is the mean entropy of gas within the Bondi radius. The Eddington rate defines the maximal inflow rate of gas not expelled by radiation pressure, as where the Bondi rate approximates the quantity of hot, ambient gas captured by the SMBH. Assuming  $K_{\text{Bon}} = K_0$ , the derived  $M_{\text{BH}}$  gives  $\dot{M}_{\text{Edd}} \approx 23 M_{\odot} \text{ yr}^{-1}$  and  $\dot{M}_{\text{Bon}} \approx 3.2 \times 10^{-4} M_{\odot} \text{ yr}^{-1}$ . Thus, the Eddington and Bondi ratios for the accretion event which powered the AGN outburst are  $\dot{M}_{\text{acc}}/\dot{M}_{\text{Edd}} \approx 0.002$  and  $\dot{M}_{\text{acc}}/\dot{M}_{\text{Bon}} \approx 300$ .

The Bondi radius for IRAS09 is unresolved ( $R_{\text{Bon}} = 9$  pc), and  $K_{\text{Bon}}$  is likely less than  $K_0$ . But, for a Bondi ratio of at least unity,  $K_{\text{Bon}}$  must be  $\lesssim 0.36$  keV cm $^2$ , lower than is measured for even galactic coronae (Sun et al. 2007). In terms of entropy,  $t_{\text{cool}} \propto K^{3/2} kT_X^{-1}$  (Donahue et al. 2006). Assuming gas close to  $R_{\text{Bon}}$  is no cooler than 0.3 keV, the accreting material will have  $t_{\text{cool}} \lesssim 10$  Myr, a factor of 100 below the shortest ICM cooling time and 1/5 the free-fall time in the core. But this creates the problem that gas close to  $R_{\text{Bon}}$  is disconnected from cooling at larger radii, breaking the feedback loop (Soker 2006). If instead cold-mode accretion dominates, then the gas which becomes fuel for the AGN is distributed in the BCG halo and falls into the BCG as a result of cooling (Pizzolato & Soker 2005, 2010). Indeed, radial filaments and gaseous substructure within 30 kpc of IRAS09 are seen down to the resolution-limit of *HST* (Armstrong et al. 1999). This may indicate the presence of cooling, overdense regions similar to the cold blobs expected in cold-mode accretion. Though Bondi accretion cannot be ruled out, it does not seem viable, and the process of cold-mode accretion appears to be more consistent with the nature of IRAS09.

## 7 QSO IRRADIATION OF THE ICM

In Figure 4, three regions of X-ray emission in excess of the best-fit SB model are highlighted. The regions are illustrative and approximate the constant SB contours used to define the spectral extraction regions. Each region is denoted by its location relative to the nucleus: northern excess (NEx), eastern excess (EEx), and western excess (WEx). The NEx and WEx appear to be part of a tenuous, arc-like filament which may be gas displaced by the NW radio jet. In other clusters, structures similar to the NEx-WEx are found to be cool rims of gas (e.g. Blanton et al. 2009), but the *Chandra* data is insufficient to determine if this is the case for IRAS09, hence we treat the NEx and WEx as separate structures.

Spectral analysis was performed on each region. A background spectrum was extracted from regions neighboring the excesses which did not show enhanced emission in the residual image. The backgrounds were scaled to correct for differences in sky area. For each region, the ungrouped source and background spectra were differenced in XSPEC to create a residual spectrum. To avoid systematically cooler best-fit temperatures resulting from low count rates (Nousek & Shue 1989), the modified Cash statistic

(Cash 1979) was used during fitting. The low signal-to-noise ratio (SN) of each spectrum precluded setting metal abundance as a free parameter when fitting a thermal model. Since the three excesses reside within the two central annuli of the abundance profile, the abundance was fixed at  $0.51 Z_{\odot}$ . The best-fit values for the spectral models are given in Table 3.

The NEx residual spectrum had low-SN which resulted in poor resolution of spectral features. Thus, the thermal model had an unconstrained temperature of  $\sim 7$  keV, and similarly the power-law model had an unconstrained spectral index of  $\Gamma \sim 1.9$ . The northern radio jet terminates in the NEx region, and the hardness ratio map (see Section 8 and Figure 4) shows a possible hot spot in this same area. The NEx may result from non-thermal emission in the hot spot, but we cannot confirm this spectroscopically.

The WEx has a residual spectrum consistent with thermal emission, but the EEx spectrum has prominent features at  $E < 2$  keV which were poorly fit by a single-component thermal model. The EEx thermal Fe K $\alpha$  complex was also poorly fit because of an obvious asymmetry toward lower energies. To reconcile the poor fit, three Gaussians were added to the EEx model. Comparison of fit statistics and goodness of fits determined from 10,000 Monte Carlo simulations of the best-fit spectra suggest the model with the Gaussians is preferred. The strength of the features relative to the continuum suggest a thermal origin is unlikely, and that the features may be emission line blends. Below we discuss the EEx exclusively.

H93 and Hines et al. (1999, hereafter H99) suggest the AGN which produced the large-scale jets has been reoriented within the last few Myrs, resulting in a new beaming direction close to the line of sight and at roughly a right angle to the previous beaming axis. Interestingly, the new AGN axis suggested by H99 is coincident with the EEx, the radio spur northeast of the radio core, a cone of UV ionization, an ionized optical nebula, and highly polarized diffuse optical emission. These respective features are outlined in Figure 4. Russell et al. (2010) demonstrate that the QSO in H1821+643, which is 2 times more luminous than IRAS09, is capable of photoionizing gas up to 30 kpc from the nucleus, and we suspect a similar process may be occurring in IRAS09.

To test this hypothesis, reflection and diffuse spectra were simulated for the nebula and ICM coincident with the EEx using CLOUDY (Ferland et al. 1998). The nebular gas density and ionization state were taken from Tran et al. (2000), while the initial ICM temperature, density, and abundance were set at 3 keV,  $0.04 \text{ cm}^{-3}$ , &  $0.51 Z_{\odot}$ , respectively. No Ca or Fe lines are detected from the nebula coincident with the EEx, but strong Mg, Ne, and O lines are (Tran et al. 2000), possibly as a result of metal depletion onto dust grains (e.g. Donahue & Voit 1993). Thus, a metal depleted, grain-rich, 12 kpc thick nebular slab was placed 15 kpc from an attenuated  $\Gamma = 1.7$  power law source with power  $1 \times 10^{47} \text{ erg s}^{-1}$ . Likewise, a  $17 \text{ kpc} \times 16 \text{ kpc}$  ICM slab was placed 19 kpc from the same source. The QSO radiation was attenuated using a 15 kpc column of density  $0.06 \text{ cm}^{-3}$ , abundance  $0.51 Z_{\odot}$ , and temperature 3 keV. The output models were summed, folded through the Chandra responses using XSPEC, and fitted to the observed EEx spectrum (shown in Figure 5).

In the energy range 0.1-10.0 keV, the nebula emission lines which exceed the thermal line emission originate from Si, Cl, O, F, K, Ne, Co, Na, & Fe and occur as blends around redshifted 0.4, 0.6, 0.9, & 1.6 keV. The energies and strengths of these blends are in good agreement with the EEx spectrum. Further, the Fe K $\alpha$  emission from the nebula is 100 times fainter than that from the ICM, and the observed asymmetry of the EEx Fe K $\alpha$  emission results

from the 6.4 keV Fe K $\alpha$  photoionized line of the ICM. It is clear that beamed QSO radiation is responsible for the nature of the EEx, but if the photoionization equates to heating of the gas is unclear. Nonetheless, we have demonstrated that QSO radiation is capable of impacting cool gas over a large angle which is far from the nucleus.

One alternative explanation for the EEx is that it is low entropy gas uplifted from deeper within the core along the new AGN beaming axis. Scattered UV emission 32 kpc from the core places a minimum lifetime of 73 kyr for the new beaming direction (H93), and, assuming saturated heat flux across the EEx surface, the evaporation time is exceedingly short,  $< 1$  Myr. These short timescales suggest the EEx was transported to the present location at  $> 20$  times the ambient sound speed, or  $v \sim 0.06\text{--}0.1c$ , well below typical jet bulk flow velocities. The radio spur has a 1.4 GHz luminosity of  $\approx 3 \times 10^{39} \text{ erg s}^{-1}$ , suggesting an associated 1 Myr old jet would have  $\sim 10^{57} \text{ erg}$  of kinetic energy, which is sufficient to lift  $\sim 10^{10} M_{\odot}$  to a distance of 19 kpc. It appears uplift is feasible, particularly if the gas is magnetically-shielded and conduction is staved-off.

## 8 NUCLEUS X-RAY EMISSION

The centroid and extent of the nuclear X-ray source were determined using the CIAO tool *wavdetect* and the Chandra PSF. Each was confirmed with a hardness ratio map calculated as  $HR = f(2.0\text{--}9.0 \text{ keV})/f(0.5\text{--}2.0 \text{ keV})$ , where  $f$  is the flux in the denoted energy band. A source extraction region was defined using the 90% enclosed energy fraction (EEF) of the normalized Chandra PSF specific to the nuclear source median photon energy and off-axis position. The elliptical source region had an effective radius of  $1.16''$ . A segmented elliptical annulus with the same central coordinates, ellipticity, and position angle as the source region, but having 5 times the area, was used for the background region. The background annulus was broken into segments to avoid the regions of excess X-ray emission discussed in Section 7. The HR map and extraction regions are shown in Figure 6.

Source and background spectra were created using the CIAO tool *psextract*. The source spectrum was grouped to have 20 counts per energy channel. The background-subtracted Chandra spectra and best-fit models are presented in Figure 6. The significant flux difference below 1.3 keV is a result of the greater effective area of the ACIS-S3 CCD in 1999 versus ACIS-I3 in 2009. Approximately 72% of the 2009 spectrum (hereafter, SP09) is from the source, with a count rate of  $1.63 (\pm 0.06) \times 10^{-2} \text{ ct s}^{-1}$  in the 0.5-9.0 keV band. For the 1999 spectrum (hereafter, SP99), 67% is source flux, with a 0.5-9.0 keV count rate of  $2.71 (\pm 0.26) \times 10^{-2} \text{ ct s}^{-1}$ . We confirm the findings of Iwasawa et al. (2001) that the ICM thermal Fe K $\alpha$  contribution to the nuclear spectrum is negligible, and that prominent, blended, line-like features around 0.8 keV and 1.3 keV are superposed on the continuum.

Previous studies have shown the nuclear spectrum is best modeled as Compton reflection from cold matter with a strong Fe K $\alpha$  fluorescence line ( $E_{\text{rest}} = 6.4 \text{ keV}$ ). The SP99 and SP09 were fitted separately in XSPEC over the energy range 0.5-7.0 keV with an absorbed PEXRAV model (Magdziarz & Zdziarski 1995) plus three Gaussians. The disk-reflection geometry employed in the PEXRAV model is not ideal for fitting reflection from a Compton-thick torus (Murphy & Yaqoob 2009), but no other suitable XSPEC model is currently available. Hence, only the PEXRAV reflection component was fitted and no high energy cut-off for the power law was used.



Fitting separate SP99 and SP09 models allowed for source variation in the decade between observations, however  $\Gamma$  was poorly constrained for SP99 and thus fixed at the SP09 value. Using constraints from Tran et al. (2000), the model parameters for reflector abundance and source inclination were fixed at  $1.0 Z_{\odot}$  and  $i = 50^{\circ}$ , respectively. Setting abundance as a free parameter did not statistically improve the fits. The best-fit model parameters are presented in Table 4.

Using a solar abundance thermal component in place of the two low-energy Gaussians yielded a statistically worse fit. The model systematically underestimated the 1-1.5 keV flux and overestimated the 2-4 keV flux. Leaving the thermal component abundance as a free parameter resulted in  $0.1 Z_{\odot}$ , *i.e.* the thermal component tended toward a featureless skewed-Gaussian. Strong Mg, Ne, S, and Si K $\alpha$  fluorescence lines at  $E < 3.0$  keV can be present in reflection spectra (George & Fabian 1991), as can Fe L-shell lines from photoionized gas (Band et al. 1990). We conclude that the soft X-ray emission modeled using the Gaussians is likely a combination of emission line blends and low-level thermal continuum, whether the thermal component is nuclear or ambient in origin is unclear.

The unabsorbed 2-10 keV *reflected* flux is  $4.24^{+0.57}_{-0.55} \times 10^{-13}$  erg s $^{-1}$  cm $^{-2}$  corresponding to a rest-frame  $L_{2-10} = 1.57^{+0.19}_{-0.19} \times 10^{44}$  erg s $^{-1}$ . Adjusted for cosmology, this agrees with the measurement from Iwasawa et al. (2001). Since we have used a pure reflection model, the intrinsic QSO luminosity can only be estimated as  $(\kappa/\eta)L_{2-10}$  where  $\kappa = 40$  is a bolometric correction factor (Vasudevan & Fabian 2007) and  $\eta = 0.06$  is the reflector albedo (Murphy & Yaqoob 2009). This gives  $L_{\text{bol}}^{\text{QSO}} = 1.05 (\pm 0.13) \times 10^{47}$  erg s $^{-1}$ .

As a check for acceptable agreement between our models and results of prior studies, the  $R_{500}$  Chandra, XMM-Newton, and BeppoSAX spectra were jointly fitted with our best-fit nucleus and ICM models simultaneously. There were no significant differences between our models and those of Franceschini et al. (2000), Iwasawa et al. (2001), and the Piconcelli et al. (2007) reflection model. The value for the Fe K $\alpha$  equivalent width ( $\text{EW}_{\text{K}\alpha}$ ), which is a valuable diagnostic for probing the environment of an AGN (see Fabian et al. 2000a, for a review), also agrees with previous measurements which found  $\text{EW}_{\text{K}\alpha} \lesssim 1$  keV. The large uncertainties associated with the individual SP99, XMM-Newton, and BeppoSAX  $\text{EW}_{\text{K}\alpha}$  values prevents us from determining if  $\text{EW}_{\text{K}\alpha}$  has varied since 1998.

Our results are consistent with models and observations which show that  $\text{EW}_{\text{K}\alpha} \gtrsim 0.5$  keV is correlated with  $\Gamma \gtrsim 1.7$  and reflecting column densities  $N_{\text{H,ref}} \sim 10^{24}$  cm $^{-2}$  (Matt et al. 1996; Nandra et al. 1997; Zdziarski et al. 1999; Guainazzi et al. 2005). Previous studies suggested the BeppoSAX PDS detection resulted primarily from transmission of hard X-rays through an obscuring screen with  $N_{\text{H,obs}} > 10^{24}$  cm $^{-2}$ . Extrapolating our best-fit model out to 10-80 keV reveals statistically acceptable agreement with the PDS data (see Figure 4). The 10-200 keV model flux is  $f_{10-200} = 8.15^{+0.21}_{-0.19} \times 10^{-12}$  erg s $^{-1}$  cm $^{-2}$ , which is not significantly different from the  $f_{10-200}$  measured with BeppoSAX. Addition of a second power-law component ( $\Gamma = 1.7$ ) absorbed by a  $N_{\text{H,obs}} = 3 \times 10^{24}$  cm $^{-2}$  screen at the IRAS09 redshift to the model lowered  $\chi^2$  but with no statistical improvement to the fit. If transmitted hard X-ray emission falls within the passband used for spectral analysis,  $\Gamma$  would be artificially lowered, and the extrapolated hard X-ray flux thus increases. However, for  $\Gamma \geq 1.7$ , column densities  $> 3 \times 10^{24}$  cm $^{-2}$  are sufficient to suppress significant transmit-

ted emission below the 7 keV spectral analysis cut-off, indicating the best-fit model should not have an artificially low  $\Gamma$ .

That we find no need for an additional hard X-ray component does not contradict the well-founded conclusion that IRAS09 harbors a Compton-thick QSO. On the contrary, the measured  $\text{EW}_{\text{K}\alpha}$  suggests reflecting column densities of  $N_{\text{H,ref}} \sim 1-5 \times 10^{24}$  cm $^{-2}$  (Leahy & Creighton 1993; Guainazzi et al. 2005; Comastri et al. 2010). Assuming the density of material surrounding the QSO is mostly homogeneous, *i.e.*  $N_{\text{H,ref}} \approx N_{\text{H,obs}}$ , our results are consistent with the presence of a moderately Compton-thick screen.

## 9 EVOLUTION OF THE FEEDBACK MODE?

Cosmological simulations typically segregate radiatively- and mechanically-dominated feedback into a distinct early-time quasar-mode (*e.g.* Springel et al. 2005) and a late-time radio-mode (*e.g.* Croton et al. 2006), respectively. These modes of feedback are used to ensure that SMBH-host galaxy co-evolution is in accordance with observations (*e.g.* Magorrian et al. 1998). The quasar-mode is expected to be brief, expelling large quantities of cold gas from the host galaxy (Narayanan et al. 2006); whereas the radio-mode is prolonged & intermittent, heating the extended hot halo such that future cooling is regulated (see McNamara & Nulsen 2007, for a review). There are numerous examples of systems dominated by mechanical feedback (*e.g.* Fabian et al. 2000b; McNamara et al. 2005), and there are indications that many high-redshift galaxies are dominated by QSO feedback (see Veilleux et al. 2005, for a review), but in a unified feedback model, there must be a transition from the dominance of one mode to the other, and we suspect IRAS09 is one such example. But aside from the obvious AGN mechanical feedback and irradiation of the ICM by the QSO, are there other indications of quasar-mode feedback in the host galaxy which would strengthen the case?

The  $\text{H}_2$  mass of IRAS09 is  $< 10^{10} M_{\odot}$  (Evans et al. 1998), there is  $< 10^8 M_{\odot}$  of cold dust (Deane & Trentham 2001), no polycyclic aromatic hydrocarbon or silicate absorption features are detected (Peeters et al. 2004; Sargsyan et al. 2008), and the hot dust mass is  $\sim 10^9 M_{\odot}$  (Taniguchi et al. 1997). Additionally, the  $\text{H}\alpha$  luminosity exceeds  $10^{42}$  erg s $^{-1}$  (Crawford & Vanderriest 1996; Evans et al. 1998). Based on these measurements, and compared with other BCGs (*e.g.* Edge 2001), IRAS09 appears to be gas-poor with a low gas-to-dust ratio. All told, the lack of strong molecular gas indicators around such a powerful QSO is odd. One possible explanation for the discrepancy is that the QSO is driving gas out of the galaxy via non-relativistic winds, radiation pressure, or a combination of both (*e.g.* Hopkins & Elvis 2010). Indeed, integral field spectroscopy indicates the presence of a  $> 1000$  km s $^{-1}$  emission line outflow coincident with the nucleus (Crawford & Vanderriest 1996). Further, the CO observations used to infer the  $\text{H}_2$  mass (Evans et al. 1998) were not sensitive to velocities  $> 300$  km s $^{-1}$ , the regime where molecular gas being expelled at high-velocities ( $\sim 1000$  km s $^{-1}$ ) by QSO winds might be detected. Given that rapid & extensive dust formation is also expected in such QSO winds (Elvis et al. 2002), this may further explain the extreme dust richness of IRAS09.

Fabian et al. (2009, hereafter F09) show that QSO/AGN radiation pressure has a significant influence on dusty material in the host galaxy. F09 define the effective Eddington ratio for dusty gas to be  $\lambda_{\text{Edd}} = L_{\text{bol}}^{\text{QSO}} (1.38 \times 10^{38} M_{\text{BH}})^{-1}$ , and for IRAS09, this has a value of  $\approx 0.72$ . F09 also present a plane for  $N_{\text{H,obs}} - \lambda_{\text{Edd}}$  which is divided into regions where obscuring clouds are either long-lived

or experience the effects of a super-Eddington AGN, *i.e.* where clouds are efficiently expelled. In this plane, IRAS09 resides near the boundary of the two regions, close enough that it is reasonable to suspect that the massive reservoir of dust-laden gas in the galaxy is being heated, ionized, or accelerated away from the QSO by radiation pressure. These conclusions are, however, at the mercy of our choice for  $M_{\text{BH}}$ , *i.e.* if  $M_{\text{BH}} \geq 5 \times 10^9 M_{\odot}$ , then  $\lambda_{\text{Edd}} < 0.2$ , as where  $M_{\text{BH}} < 1 \times 10^9 M_{\odot}$  implies  $\lambda_{\text{Edd}} > 1$ .

All three of the primary channels for QSO/AGN feedback to influence its environment (jets, winds, radiation) are conceivably active in IRAS09, and it may be that these processes are simultaneously conspiring to quench cooling within and around the host galaxy. ~~But are we really witnessing the evolution from one dominant form of feedback to another?~~ The mass accretion rate required to power the QSO is  $\dot{M}_{\text{acc}} = L_{\text{bol}}^{\text{QSO}} / (0.1c^2) \approx 20 M_{\odot} \text{ yr}^{-1}$ , 300 times larger than  $\dot{M}_{\text{acc}}$  needed to power the jets. At this rate, the black hole mass will double in  $\approx 50$  Myr, and for the Magorrian relation to hold,  $> 10^{11} M_{\odot}$  of stars would need to form,  $> 10\%$  of the current bulge mass. This seems unlikely, and thus the current period of QSO activity ~~should be fleeting, giving way to a sustained period of sub-Eddington accretion which can readily power an AGN but not its hulking brother the QSO.~~ The emergence of jets may have signaled this change. Further, H93 and H99 discuss in detail that the misalignment between the large-scale radio jets and beamed nuclear radiation may be correlated with evolution of the radio source from a FR-II to FR-I, and that the jet axis realignment must have transpired in less than a few Myrs. ~~The origin of the misalignment cannot be determined with any certainty, but one can speculate.~~

~~In the following discussion we assume the axes of an AGN jet and SMBH spin are one in the same.~~ One simple explanation is that there are multiple SMBHs in the nucleus, each with their own accretion system but isotropic spin axes. ~~Hence there is no misalignment, we are seeing emission from two separate systems: one turning on, one turning off.~~ Another explanation is that a single SMBH has undergone a “spin-flip” (Merritt & Ekers 2002) when a smaller black hole merged with it. BCGs are known for cannibalism, and 6 suspected companion galaxies reside within a projected 80 kpc of the BCG (Soifer et al. 1996; Armus et al. 1999), so it is not out of the question that one or more mergers have taken place in the last few Myrs. However, black hole mergers are lengthy (few Gyrs) and difficult processes, and the spin axes of the merging black holes may naturally align when in a gas-rich environment (Bogdanović et al. 2007).

Based on the spin evolution framework of Garofalo et al. (2010), there is yet another intriguing explanation which does not specifically require mergers to alter the SMBH spin axis. Garofalo et al. (2010) suggest that evolution of a black hole spin state from retrograde to prograde relative to accreting matter is specifically correlated with a transition of the radio source from a powerful FR-II to a low-power FR-I. During the process of retrograde spin-down, the black hole must pass through a state where the spin is  $\approx 0$ . At this point, if there is an asymmetric accretion flow exceeding a  $M_{\text{BH}}$ -dependent critical  $\dot{M}_{\text{acc}}$ , the spin axis can be dramatically reoriented on timescales of a few Myrs (Cavagnolo et al., in preparation), possibly giving rise to the type of jet-beamed radiation misalignment observed in IRAS09. This process may also accompany quenching of the cold gas reservoir in the host galaxy, hastening the transition from quasar-dominated to radio-dominated feedback.

## 10 SUMMARY

In this paper we have shown, through a new *Chandra* X-ray observation, that the AGN/QSO in IRAS 09104+4109 is interacting with the ICM of RX J0913.7+4056 through both the mechanical and radiative feedback channels. The results presented in this paper are as follows:

- The RX J0913.7+4056 ICM global and radial properties reveal no signs of shocks, cold fronts, a radio halo, or deviations from hydrostatic equilibrium to suggest disruption by a major merger or prior cluster-scale AGN outburst. RX J0913.7+4056 is an unremarkable, massive, cool-core galaxy cluster with a 12 keV  $\text{cm}^2$  core entropy, mass that scales as  $T_{\text{cl}}^{3/2}$ , and a mean cluster gas fraction of 0.11.

- We have discovered cavities in the X-ray halo of IRAS09 which indicate an AGN outburst with total mechanical power of at least  $3 \times 10^{44} \text{ erg s}^{-1}$  and total energy output of  $6 \times 10^{59} \text{ erg}$ . Comparison of the cavity sound speed ages and radio source ages indicate the outflow may be supersonic, and if significant gas shocking has occurred, the total kinetic power of the AGN may be  $\sim 10^{46} \text{ erg s}^{-1}$ .

- Core ICM properties and the mass accretion rate required to power the AGN outburst suggest that fuel for the AGN was likely not accreted directly from the hot ICM, *i.e.* via the Bondi mechanism, but rather attained through cold-mode accretion. This conclusion is consistent with the sub-kpc structure of the BCG halo and the X-ray properties of the nucleus.

- Detection of an X-ray excess 13-26 kpc NE of the nucleus indicates beamed radiation from the  $\sim 10^{47} \text{ erg s}^{-1}$  QSO is escaping the nucleus and interacting with the ICM in the same region as a strongly photoionized nebulae. The X-ray emission properties of this region are well-fit by a model where the nebula and ICM are being irradiated by the QSO.

- The nuclear X-ray source is well-fit by a reflection-dominated model where the power law source is obscured by moderately Compton-thick material. The width of the nuclear Fe K $\alpha$  fluorescence emission line indicates a reflecting column density, and presumably obscuring column density, of  $> 10^{24} \text{ cm}^{-2}$ . We also show that the *BeppoSAX* PDS detection of hard X-ray emission can also be explained by reflected emission.

- Based on the ostensible IRAS09 gas-poorness, nuclear emission line outflow, high effective Eddington QSO luminosity which can expel clouds, and misalignment of the large-scale radio jets & beamed radiation from the nucleus, we suggest that IRAS09 is evolving from a radiation-dominated mode of feedback to a kinetic-dominated mode. Among other possible explanations, we speculate that the observed properties of IRAS09 may be related to the process of SMBH spin evolution. IRAS09 may be a local example of how massive galaxies at higher redshifts evolve from quasar-mode into radio-mode.

## ACKNOWLEDGEMENTS

KWC and MD were supported by SAO grant GO9-0143X, and MD and GMV acknowledges support through NASA LTSA grant NASA NNG-05GD82G. KWC and BRM thank the Natural Sciences and Engineering Research Council of Canada for support. KWC thanks Alastair Edge & Niayesh Afshordi for helpful insight, and Guillaume Belanger & Roland Walter for advice regarding *INTEGRAL* data analysis.



## REFERENCES

- Allen S. W., 2000, *MNRAS*, 315, 269 [3](#)
- Anders E., Grevesse N., 1989, *Geochim. Cosmochim. Acta*, 53, 197 [1](#)
- Armus L., Soifer B. T., Neugebauer G., 1999, *Ap&SS*, 266, 113 [5, 8](#)
- Arnaud K. A., 1996, in *Astronomical Society of the Pacific Conference Series*, Vol. 101, *Astronomical Data Analysis Software and Systems V*, Jacoby G. H., Barnes J., eds., pp. 17–+ [1](#)
- Arnaud M., Aghanim N., Neumann D. M., 2002, *A&A*, 389, 1 [3](#)
- Band D. L., Klein R. I., Castor J. I., Nash J. K., 1990, *ApJ*, 362, 90 [7](#)
- Bassani L., Molina M., Malizia A., Stephen J. B., Bird A. J., Bazzano A., Bélanger G., Dean A. J., De Rosa A., Laurent P., Lebrun F., Ubertini P., Walter R., 2006, *ApJ*, 636, L65 [2](#)
- Bîrzan L., McNamara B. R., Nulsen P. E. J., Carilli C. L., Wise M. W., 2008, *ApJ*, 686, 859 [4](#)
- Bîrzan L., Rafferty D. A., McNamara B. R., Wise M. W., Nulsen P. E. J., 2004, *ApJ*, 607, 800 [4](#)
- Blanton E. L., Randall S. W., Douglass E. M., Sarazin C. L., Clarke T. E., McNamara B. R., 2009, *ApJ*, 697, L95 [5](#)
- Bogdanović T., Reynolds C. S., Miller M. C., 2007, *ApJ*, 661, L147 [8](#)
- Carilli C. L., Perley R. A., Dreher J. W., Leahy J. P., 1991, *ApJ*, 383, 554 [3](#)
- Cash W., 1979, *ApJ*, 228, 939 [6](#)
- Cavagnolo K. W., Donahue M., Voit G. M., Sun M., 2008a, *ApJ*, 683, L107 [4](#)
- , 2008b, *ApJ*, 682, 821 [4](#)
- , 2009, *ApJS*, 182, 12 [4](#)
- Cavaliere A., Fusco-Femiano R., 1978, *A&A*, 70, 677 [3](#)
- Cohen A. S., Lane W. M., Cotton W. D., Kassim N. E., Lazio T. J. W., Perley R. A., Condon J. J., Erickson W. C., 2007, *AJ*, 134, 1245 [2](#)
- Comastri A., Iwasawa K., Gilli R., Vignali C., Ranalli P., Matt G., Fiore F., 2010, *ArXiv e-prints* [7](#)
- Crawford C. S., Vnderriest C., 1996, *MNRAS*, 283, 1003 [5, 7](#)
- Croton D. J., Springel V., White S. D. M., De Lucia G., Frenk C. S., Gao L., Jenkins A., Kauffmann G., Navarro J. F., Yoshida N., 2006, *MNRAS*, 365, 11 [7](#)
- Deane J. R., Trentham N., 2001, *MNRAS*, 326, 1467 [7](#)
- Diehl S., Statler T. S., 2006, *MNRAS*, 368, 497 [4](#)
- Donahue M., Horner D. J., Cavagnolo K. W., Voit G. M., 2006, *ApJ*, 643, 730 [5](#)
- Donahue M., Voit G. M., 1993, *ApJ*, 414, L17 [6](#)
- Edge A. C., 2001, *MNRAS*, 328, 762 [7](#)
- Elvis M., Marengo M., Karovska M., 2002, *ApJ*, 567, L107 [7](#)
- Evans A. S., Sanders D. B., Cutri R. M., Radford S. J. E., Surace J. A., Solomon P. M., Downes D., Kramer C., 1998, *ApJ*, 506, 205 [1, 7](#)
- Faber S. M., Jackson R. E., 1976, *ApJ*, 204, 668 [5](#)
- Fabian A. C., Crawford C. S., 1995, *MNRAS*, 274, L63 [4](#)
- Fabian A. C., Iwasawa K., Reynolds C. S., Young A. J., 2000a, *PASP*, 112, 1145 [7](#)
- Fabian A. C., Sanders J. S., Etori S., Taylor G. B., Allen S. W., Crawford C. S., Iwasawa K., Johnstone R. M., Ogle P. M., 2000b, *MNRAS*, 318, L65 [7](#)
- Fabian A. C., Shioya Y., Iwasawa K., Nandra K., Crawford C., Johnstone R., Kunieda H., McMahon R., Makishima K., Murayama T., Ohashi T., Tanaka Y., Taniguchi Y., Terashima Y., 1994, *ApJ*, 436, L51 [1](#)
- Fabian A. C., Vasudevan R. V., Mushotzky R. F., Winter L. M., Reynolds C. S., 2009, *MNRAS*, 394, L89 [7](#)
- Ferland G. J., Korista K. T., Verner D. A., Ferguson J. W., Kingdon J. B., Verner E. M., 1998, *PASP*, 110, 761 [6](#)
- Ferrari C., Govoni F., Schindler S., Bykov A. M., Rephaeli Y., 2008, *Space Science Reviews*, 134, 93 [3](#)
- Franceschini A., Bassani L., Cappi M., Granato G. L., Malaguti G., Palazzi E., Persic M., 2000, *A&A*, 353, 910 [1, 2, 7](#)
- Garofalo D., Evans D. A., Sambruna R. M., 2010, *ArXiv e-prints* [8](#)
- George I. M., Fabian A. C., 1991, *MNRAS*, 249, 352 [7](#)
- Graham A. W., 2007, *MNRAS*, 379, 711 [5](#)
- Guainazzi M., Matt G., Perola G. C., 2005, *A&A*, 444, 119 [7](#)
- Heavens A. F., Meisenheimer K., 1987, *MNRAS*, 225, 335 [3](#)
- Hines D. C., Schmidt G. D., Wills B. J., Smith P. S., Sowers L. G., 1999, *ApJ*, 512, 145 [6, 15](#)
- Hines D. C., Wills B. J., 1993, *ApJ*, 415, 82 [1, 2](#)
- Hopkins P. F., Elvis M., 2010, *MNRAS*, 401, 7 [7](#)
- Iwasawa K., Fabian A. C., Etori S., 2001, *MNRAS*, 321, L15 [1, 6, 7](#)
- Jaffe W. J., Perola G. C., 1973, *A&A*, 26, 423 [3](#)
- Kalberla P. M. W., Burton W. B., Hartmann D., Arnal E. M., Bajaja E., Morras R., Pöppel W. G. L., 2005, *A&A*, 440, 775 [1](#)
- Kardashev N. S., 1962, *Soviet Astronomy*, 6, 317 [3](#)
- Kleinmann S. G., Hamilton D., Keel W. C., Wynn-Williams C. G., Eales S. A., Becklin E. E., Kuntz K. D., 1988, *ApJ*, 328, 161 [1](#)
- Kriss G. A., Cioffi D. F., Canizares C. R., 1983, *ApJ*, 272, 439 [4](#)
- Leahy D. A., Creighton J., 1993, *MNRAS*, 263, 314 [7](#)
- Magdziarz P., Zdziarski A. A., 1995, *MNRAS*, 273, 837 [6](#)
- Magorrian J., Tremaine S., Richstone D., Bender R., Bower G., Dressler A., Faber S. M., Gebhardt K., Green R., Grillmair C., Kormendy J., Lauer T., 1998, *AJ*, 115, 2285 [7](#)
- Matt G., Brandt W. N., Fabian A. C., 1996, *MNRAS*, 280, 823 [7](#)
- Maughan B. J., 2007, *ApJ*, 668, 772 [3](#)
- McNamara B. R., Nulsen P. E. J., 2007, *ARA&A*, 45, 117 [4, 7](#)
- McNamara B. R., Nulsen P. E. J., Wise M. W., Rafferty D. A., Carilli C., Sarazin C. L., Blanton E. L., 2005, *Nature*, 433, 45 [7](#)
- Merritt D., Ekers R. D., 2002, *Science*, 297, 1310 [8](#)
- Mewe R., Gronenschild E. H. B. M., van den Oord G. H. J., 1985, *A&AS*, 62, 197 [1](#)
- Miley G., 1980, *ARA&A*, 18, 165 [3](#)
- Murphy K. D., Yaqoob T., 2009, *MNRAS*, 397, 1549 [6, 7](#)
- Nandra K., George I. M., Mushotzky R. F., Turner T. J., Yaqoob T., 1997, *ApJ*, 477, 602 [7](#)
- Narayanan D., Cox T. J., Robertson B., Davé R., Di Matteo T., Hernquist L., Hopkins P., Kulesa C., Walker C. K., 2006, *ApJ*, 642, L107 [7](#)
- Nousek J. A., Shue D. R., 1989, *ApJ*, 342, 1207 [5](#)
- Pacholczyk A. G., 1970, *Radio astrophysics. Nonthermal processes in galactic and extragalactic sources*, Pacholczyk A. G., ed. [3](#)
- Paturel G., Petit C., Prugniel P., Theureau G., Rousseau J., Brouty M., Dubois P., Cambrésy L., 2003, *A&A*, 412, 45 [5](#)
- Peeters E., Spoon H. W. W., Tielens A. G. G. M., 2004, *ApJ*, 613, 986 [7](#)
- Piconcelli E., Fiore F., Nicastro F., Mathur S., Brusa M., Comastri A., Puccetti S., 2007, *A&A*, 473, 85 [2, 7](#)
- Pizzolato F., Soker N., 2005, *ApJ*, 632, 821 [5](#)
- , 2010, *ArXiv e-prints* [5](#)
- Pratt G. W., Croston J. H., Arnaud M., Böhringer H., 2009, *A&A*, 498, 361 [3](#)

- Rafferty D. A., McNamara B. R., Nulsen P. E. J., 2008, *ApJ*, 687, 899 [4](#)
- Reiprich T. H., Böhringer H., 2002, *ApJ*, 567, 716 [3](#)
- Rengelink R. B., Tang Y., de Bruyn A. G., Miley G. K., Bremer M. N., Roettgering H. J. A., Bremer M. A. R., 1997, *A&AS*, 124, 259 [2](#)
- Riley J. M. W., Waldram E. M., Riley J. M., 1999, *MNRAS*, 306, 31 [2](#)
- Russell H. R., Fabian A. C., Sanders J. S., Johnstone R. M., Blundell K. M., Brandt W. N., Crawford C. S., 2010, *MNRAS*, 402, 1561 [6](#)
- Sanders J. S., 2006, *MNRAS*, 371, 829 [4](#)
- Sargsyan L., Mickaelian A., Weedman D., Houck J., 2008, *ApJ*, 683, 114 [7](#)
- Scheuer P. A. G., Williams P. J. S., 1968, *ARA&A*, 6, 321 [3](#)
- Slee O. B., Roy A. L., Murgia M., Andernach H., Ehle M., 2001, *AJ*, 122, 1172 [3](#)
- Soifer B. T., Neugebauer G., Armus L., Shupe D. L., 1996, *AJ*, 111, 649 [8](#)
- Soker N., 2006, *New Astronomy*, 12, 38 [5](#)
- Springel V., White S. D. M., Jenkins A., Frenk C. S., Yoshida N., Gao L., Navarro J., Thacker R., Croton D., Helly J., Peacock J. A., Cole S., Thomas P., Couchman H., Evrard A., Colberg J., Pearce F., 2005, *Nature*, 435, 629 [7](#)
- Sun M., Jones C., Forman W., Vikhlinin A., Donahue M., Voit M., 2007, *ApJ*, 657, 197 [5](#)
- Taniguchi Y., Sato Y., Kawara K., Murayama T., Mouri H., 1997, *A&A*, 318, L1 [7](#)
- Tran H. D., Cohen M. H., Villar-Martin M., 2000, *AJ*, 120, 562 [5](#), [6](#), [7](#)
- Tremaine S., Gebhardt K., Bender R., Bower G., Dressler A., Faber S. M., Filippenko A. V., Green R., Grillmair C., Ho L. C., Kormendy J., Lauer T. R., Magorrian J., Pinkney J., Richstone D., 2002, *ApJ*, 574, 740 [5](#)
- Tueller J., Baumgartner W. H., Markwardt C. B., Skinner G. K., Mushotzky R. F., Ajello M., Barthelmy S., Beardmore A., Brandt W. N., Burrows D., Chincarini G., Campana S., Cummings J., Cusumano G., Evans P., Fenimore E., Gehrels N., Godet O., Grupe D., Holland S., Kennea J., Krimm H. A., Koss M., Moretti A., Mukai K., Osborne J. P., Okajima T., Pagani C., Page K., Palmer D., Parsons A., Schneider D. P., Sakamoto T., Sambruna R., Sato G., Stamatikos M., Strohm M., Ukwata T., Winter L., 2010, *ApJS*, 186, 378 [2](#)
- Vasudevan R. V., Fabian A. C., 2007, *MNRAS*, 381, 1235 [7](#)
- Veilleux S., Cecil G., Bland-Hawthorn J., 2005, *ARA&A*, 43, 769 [7](#)
- Vikhlinin A., Kravtsov A., Forman W., Jones C., Markevitch M., Murray S. S., Van Speybroeck L., 2006, *ApJ*, 640, 691 [3](#)
- Vikhlinin A., Markevitch M., Murray S. S., Jones C., Forman W., Van Speybroeck L., 2005, *ApJ*, 628, 655 [4](#)
- Voit G. M., Cavagnolo K. W., Donahue M., Rafferty D. A., McNamara B. R., Nulsen P. E. J., 2008, *ApJ*, 681, L5 [4](#)
- Waters C. Z., Zepf S. E., 2005, *ApJ*, 624, 656 [3](#)
- Zdziarski A. A., Lubinski P., Smith D. A., 1999, *MNRAS*, 303, L11 [7](#)

**Table 1.** SUMMARY OF GLOBAL ICM SPECTRAL FITS.

Region	$R_{\text{in}}$	$R_{\text{out}}$	$kT_X$	$L_{\text{bol}}$	$Z$	$\chi^2_{\text{red.}}$	D.O.F.	% Source	$\eta$	Ct. Rate
-	kpc	kpc	keV	$10^{44} \text{ erg s}^{-1}$	$Z_{\odot}$	-	-	-	$10^{-4} \text{ cm}^{-5}$	$\text{ct s}^{-1}$
(1)	(2)	(3)	(4)	(5)	(6)	(7)	(8)	(9)	(10)	(11)
$R_{200}\text{--Core}$	174	1835	$10.22^{+5.38}_{-2.65}$	$7.95^{+1.50}_{-1.80}$	$0.38^{\dagger}$	1.13	429	15	$8.50^{+4\%}_{-4\%}$	0.066
$R_{500}\text{--Core}$	174	1160	$7.54^{+1.76}_{-1.15}$	$6.90^{+0.61}_{-0.59}$	$0.38^{+0.31}_{-0.17}$	1.01	277	27	$8.24^{+6\%}_{-6\%}$	0.063
$R_{1000}\text{--Core}$	174	820	$6.80^{+1.14}_{-0.88}$	$6.17^{+0.41}_{-0.57}$	$0.38^{\dagger}$	1.05	219	38	$7.90^{+3\%}_{-3\%}$	0.058
$R_{2500}\text{--Core}$	174	519	$7.18^{+1.25}_{-0.93}$	$5.18^{+0.41}_{-0.38}$	$0.38^{\dagger}$	1.06	150	56	$6.48^{+3\%}_{-3\%}$	0.048
$R_{5000}\text{--Core}$	174	367	$6.40^{+1.01}_{-0.80}$	$3.80^{+0.44}_{-0.26}$	$0.38^{\dagger}$	1.01	104	67	$4.99^{+4\%}_{-3\%}$	0.036
$R_{200}$	13	1835	$6.02^{+0.45}_{-0.40}$	$25.6^{+2.7}_{-2.4}$	$0.41^{+0.10}_{-0.11}$	1.00	498	34	$34.4^{+2\%}_{-2\%}$	0.240
$R_{500}$	13	1160	$5.61^{+0.32}_{-0.30}$	$24.8^{+2.9}_{-2.5}$	$0.43^{+0.09}_{-0.08}$	0.78	357	54	$34.1^{+2\%}_{-2\%}$	0.237
$R_{1000}$	13	820	$5.49^{+0.28}_{-0.26}$	$24.2^{+2.6}_{-2.4}$	$0.40^{+0.08}_{-0.08}$	0.80	306	68	$33.8^{+2\%}_{-2\%}$	0.232
$R_{2500}$	13	519	$5.50^{+0.27}_{-0.25}$	$23.1^{+2.5}_{-2.0}$	$0.39^{+0.07}_{-0.07}$	0.82	265	83	$32.4^{+2\%}_{-2\%}$	0.222
$R_{5000}$	13	367	$5.34^{+0.25}_{-0.23}$	$21.8^{+2.1}_{-1.9}$	$0.39^{+0.07}_{-0.07}$	0.80	241	90	$30.9^{+2\%}_{-2\%}$	0.210
$R_{\text{cool}}$	13	128	$4.94^{+0.24}_{-0.22}$	$16.1^{+2.5}_{-2.0}$	$0.42^{+0.08}_{-0.08}$	0.89	208	98	$22.9^{+3\%}_{-3\%}$	0.155

A dagger ( $\dagger$ ) indicates core-excised regions fit with  $Z$  fixed at the iteratively determined value for  $R_{500}\text{--Core}$ . Bolometric luminosities were determined using a diagonalized response function over the energy range 0.01-100.0 keV with 5000 linearly spaced energy channels. Col. (1) Spectral extraction region; Col. (2) Inner radius; Col. (3) Outer radius; Col. (4) Gas temperature; Col. (5) Unabsorbed bolometric luminosity; Col. (6) Gas abundance; Col. (7) Reduced  $\chi^2$ ; Col. (8) Degrees of freedom; Col. (9) Percentage of emission attributable to source; Col. (10) Model normalization; Col. (11) Background-subtracted count rate.

**Table 2.** SUMMARY OF CAVITY PROPERTIES.

Cavity	$r$	$l$	$t_{\text{sonic}}$	$t_{\text{buoy}}$	$t_{\text{refill}}$	$pV$	$E_{\text{cav}}$	$P_{\text{cav}}$
-	kpc	kpc	$10^6 \text{ yr}$	$10^6 \text{ yr}$	$10^6 \text{ yr}$	$10^{58} \text{ ergs}$	$10^{59} \text{ ergs}$	$10^{44} \text{ ergs s}^{-1}$
(1)	(2)	(3)	(4)	(5)	(6)	(7)	(8)	(9)
NW	6.40	58.3	$50.5 \pm 7.6$	$84.1 \pm 10.3$	$158 \pm 20$	$5.78 \pm 1.07$	$2.31 \pm 0.43$	$1.45 \pm 0.35$
SE	6.81	64.0	$55.4 \pm 8.4$	$92.2 \pm 11.2$	$172 \pm 21$	$6.99 \pm 1.29$	$2.80 \pm 0.52$	$1.60 \pm 0.38$

Col. (1) Cavity location; Col. (2) Radius of excavated cylinder; Col. (3) Length of excavated cylinder; Col. (4) Sound speed age; Col. (5) Buoyant rise time age; Col. (6) Volume refilling age; Col. (7)  $pV$  work; Col. (8) Cavity enthalpy; Col. (9) Cavity power using sonic age.

**Table 3.** SUMMARY OF X-RAY EXCESSES SPECTRAL FITS.

Region	$kT_X$	$\eta$	$E_G$	$\sigma_G$	$\eta_G$	Cash	DOF
-	keV	$10^{-5} \text{ cm}^{-5}$	keV	keV	$10^{-6} \text{ cm}^{-2} \text{ s}^{-1}$	-	-
(1)	(2)	(3)	(4)	(5)	(6)	(7)	(8)
NEx	$7.00^{+79.9}_{-7.00}$	$0.43^{+1.07}_{-0.21}$	-	-	-	347	430
EEx	$3.03^{+1.19}_{-0.74}$	$5.80^{+1.07}_{-0.97}$	-	-	-	524	430
EEx	$3.68^{+3.34}_{-1.58}$	$2.73^{+0.98}_{-0.94}$	[0.89, 1.42, 4.23]	[0.04, 0.16, 3.6E-4]	[1.2, 2.0, 0.16]	384	430
EEx Bgd	$3.92^{+0.35}_{-0.31}$	$39.9^{+0.18}_{-0.17}$	-	-	-	471	430
WEx	$2.55^{+2.61}_{-0.98}$	$0.66^{+0.11}_{-0.07}$	-	-	-	387	430

Metal abundance was fixed at  $0.51 Z_{\odot}$  for all fits. Col. (1) Extraction region; Col. (2) Thermal gas temperature; Col. (3) Model normalization; Col. (4) Gaussian central energies; Col. (5) Gaussian dispersions; Col. (6) Gaussian normalizations; Col. (7) Modified Cash statistic; Col. (8) Degrees of freedom.



**Table 4.** SUMMARY OF NUCLEAR SOURCE SPECTRAL FITS.

Component (1)	Parameter (2)	2009 (3)	1999 (4)
PEXRAV	$\Gamma$	$1.71^{+0.23}_{-0.65}$	fixed to 2009
-	$\eta_P$	$8.07^{+0.64}_{-0.62} \times 10^{-4}$	$8.46^{+2.08}_{-2.12} \times 10^{-4}$
GAUSSIAN 1	$E_G$	$0.73^{+0.05}_{-0.24}$	$0.61^{+0.10}_{-0.05}$
-	$\sigma_G$	$85^{+197}_{-53}$	$97^{+150}_{-97}$
-	$\eta_G$	$8.14^{+3.74}_{-5.82} \times 10^{-6}$	$1.65^{+1.52}_{-1.00} \times 10^{-5}$
GAUSSIAN 2	$E_G$	$1.16^{+0.19}_{-0.33}$	$0.90^{+0.17}_{-0.90}$
-	$\sigma_G$	$383^{+610}_{-166}$	$506^{+314}_{-262}$
-	$\eta_G$	$1.03^{+3.22}_{-0.48} \times 10^{-5}$	$1.48^{+2.68}_{-1.16} \times 10^{-5}$
GAUSSIAN 3	$E_G$	$4.45^{+0.04}_{-0.04}$	$4.46^{+0.04}_{-0.07}$
-	$\sigma_G$	$45^{+60}_{-45}$	$31^{+94}_{-31}$
-	$\eta_G$	$2.67^{+0.91}_{-0.86} \times 10^{-6}$	$6.45^{+4.17}_{-3.69} \times 10^{-6}$
-	$EW_{K\alpha}^{corr}$	$531^{+211}_{-218}$	$1210^{+720}_{-710}$
Statistics	$\chi^2$	79.0	7.9
-	DOF	74	15

Fe  $K\alpha$  equivalent widths have been corrected for redshift. Units for parameters:  $\Gamma$  is dimensionless,  $\eta_P$  is in photons  $\text{keV}^{-1} \text{cm}^{-2} \text{s}^{-1}$ ,  $E_G$  are in keV,  $\sigma_G$  are in eV,  $\eta_G$  are in photons  $\text{cm}^{-2} \text{s}^{-1}$ ,  $EW_{corr}$  are in eV. Col. (1) XSPEC model name; Col. (2) Model parameters; Col. (3) Values for 2009 *Chandra* spectrum; Col. (4) Values for 1999 *Chandra* spectrum.

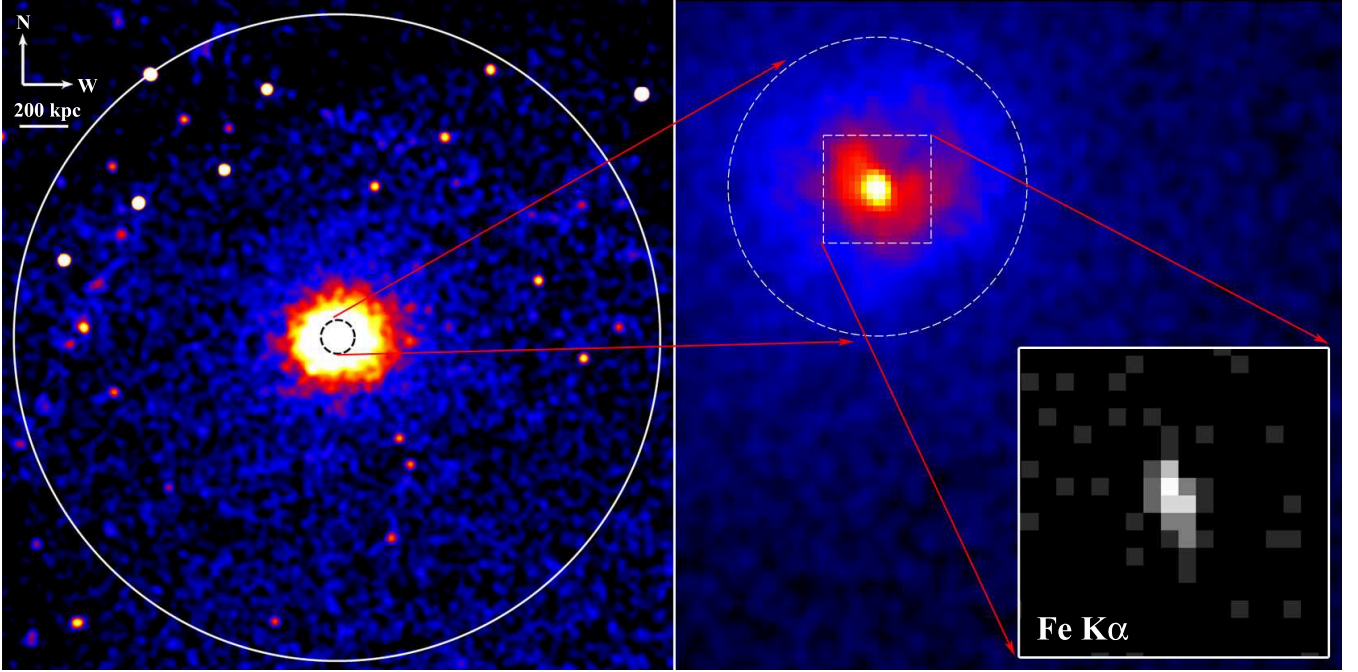


**Figure 1.** *Left:* *Chandra* 0.5–10.0 keV exposure-corrected mosaic image of the RX J0913.7+4056 ICM. Image is smoothed with 5'' Gaussian. White circle marks  $R_{500}$  and dashed region has a diameter of 140 kpc. *Right:* Zoom-in of the core region smoothed with a 1'' Gaussian. Dashed box is 25 kpc on a side. The presence of cavity like structures to the NW and SE of the nucleus are evident. *Inset:* Events in the energy range 4.35–4.5 keV associated with the redshifted Fe  $K\alpha$  fluorescence line emission from the nucleus. Areas in black have 0 ct, and the darkest gray areas have 1 ct. The extent of the source is consistent with the *Chandra* PSF, *i.e.* the source is not extended.

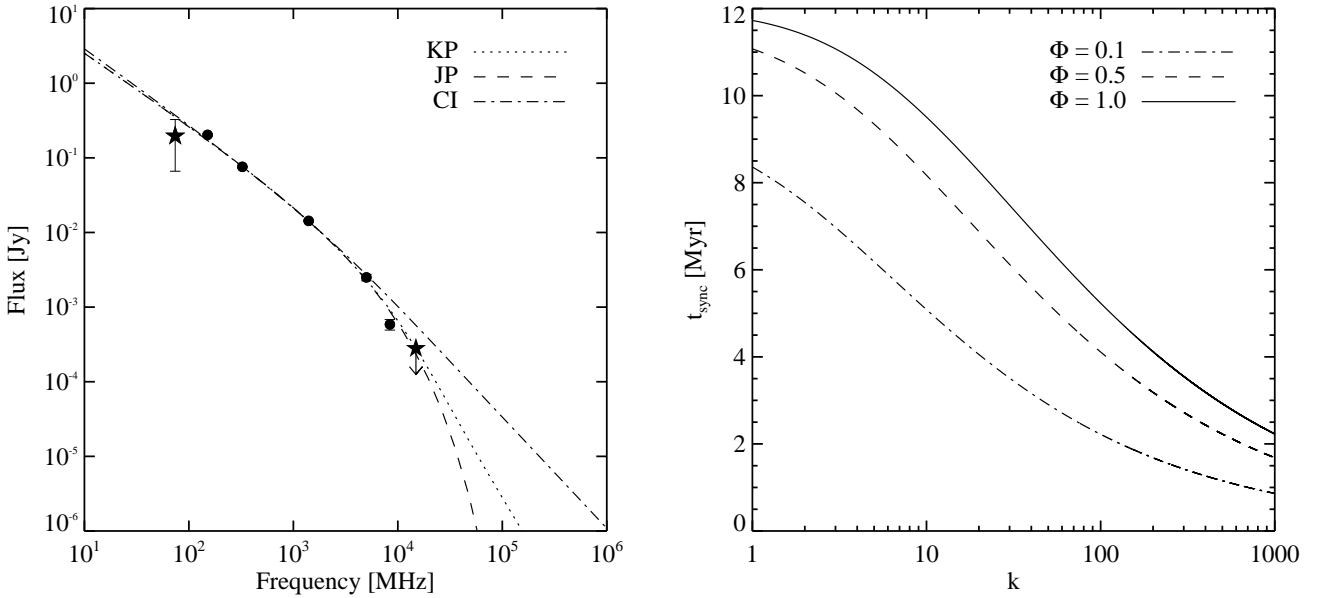


**Figure 2.** *Left:* Best-fit synchrotron models for the radio spectrum of IRAS 09104+4109. Stars denote points excluded in fitting. Plotted fluxes are for the full radio source, and the uncertainties are  $1\sigma$ . The  $1\sigma$  upper limit for the 14.9 GHz flux is shown. *Right:* Synchrotron age as a function of  $k$ , the ratio of lobe energy in non-radiating particles to that in relativistic electrons, for three values of  $\Phi$ , the volume filling factor of the radiating particle population.

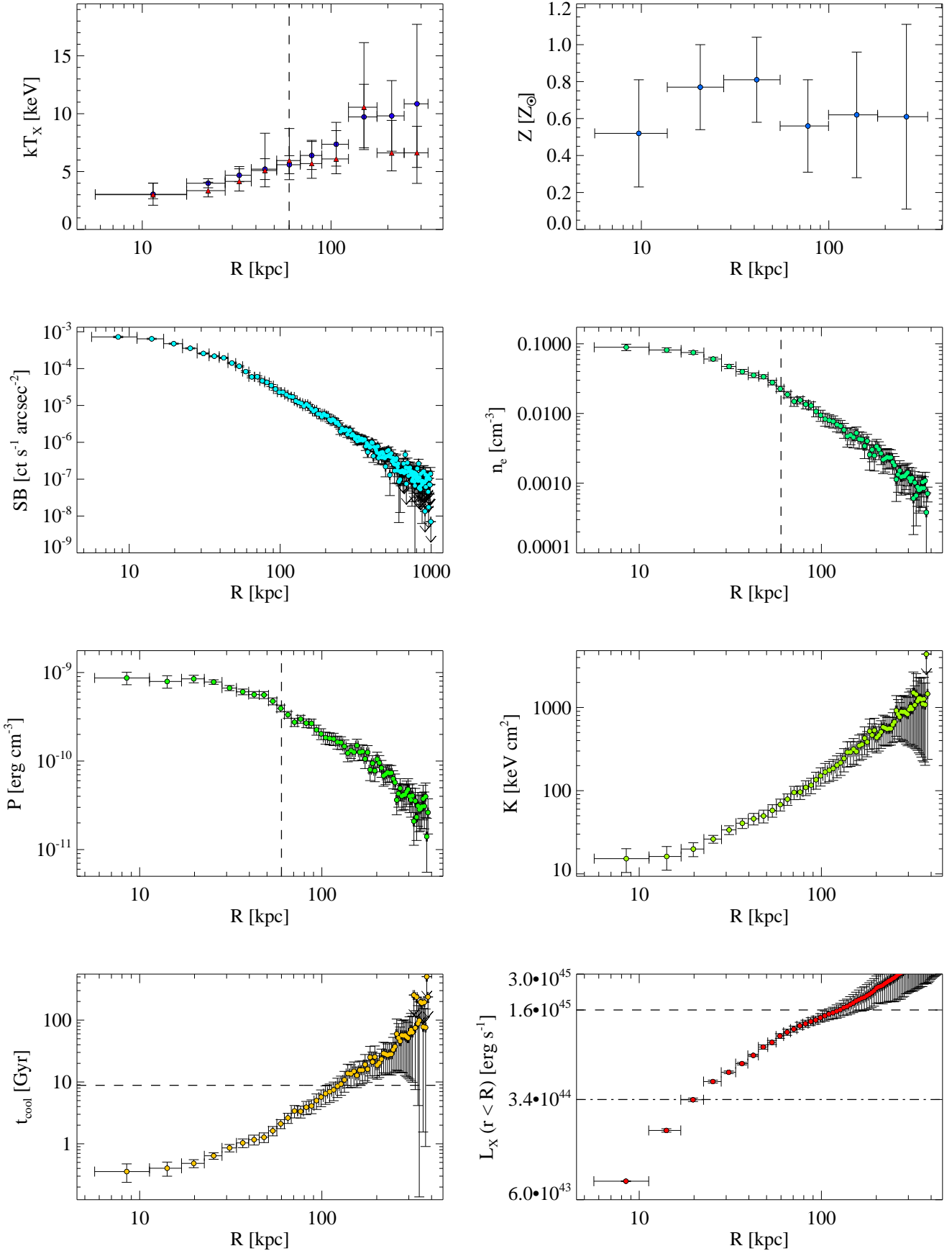


**Figure 3.** Gallery of radial ICM profiles. Vertical black dashed lines mark the approximate end-points of cavities. Horizontal dashed line in  $t_{cool}$  profile marks  $H_0^{-1}$  at  $z = 0.4418$ . For  $L_X$  profile, dashed line marks  $L_{cool}$ , and dashed-dotted line marks total  $P_{cav}$ .



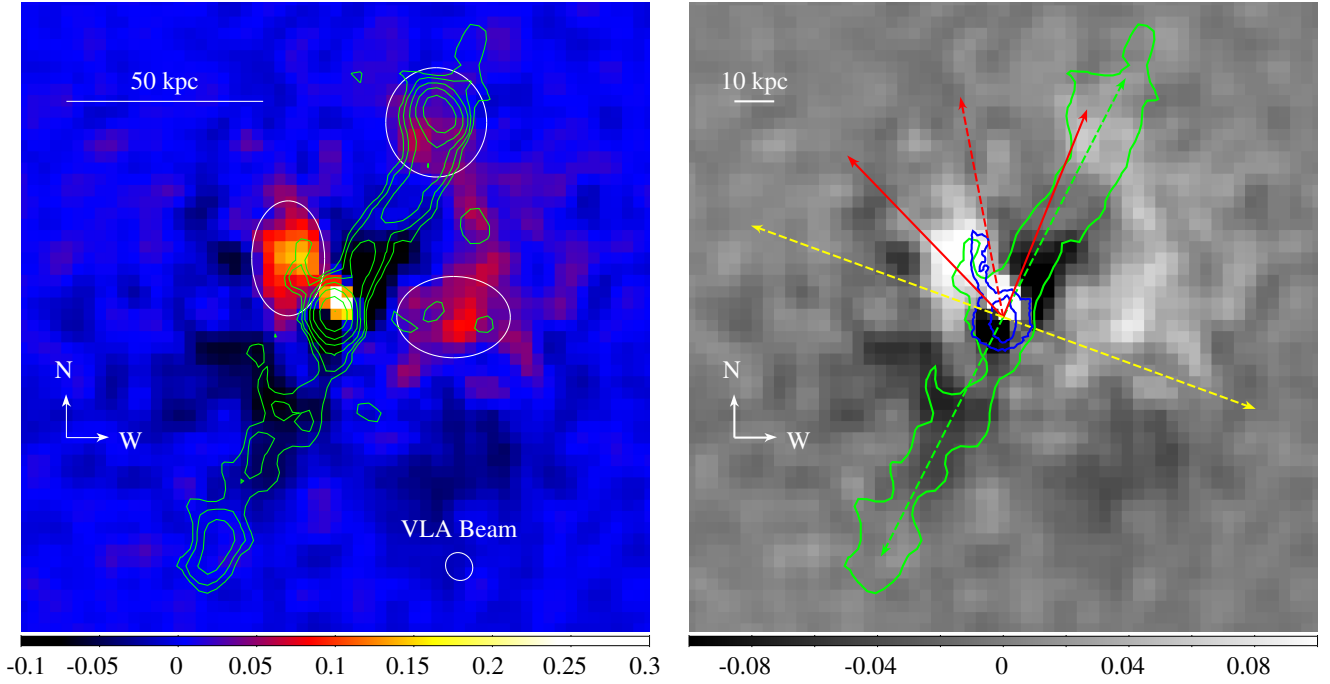


**Figure 4.** *Left:* Residual *Chandra* X-ray. Green contours trace 1.4 GHz radio emission in log-space steps beginning at  $3\sigma_{RMS}$  and ending at  $4.7 \text{ mJy beam}^{-1}$ . The three white ellipses highlight regions of interest which are discussed in Section 7. *Right:* Same residual X-ray image as left panel, but in grayscale. The green contour traces 1.4 GHz radio emission at  $3\sigma_{RMS}$ , and the dashed green line shows the jet axis. Blue contours trace  $\lambda_{rest} \approx 3900 - 6650 \text{ \AA}$  emission as seen with *HST*. The red dashed line shows the mean direction of the UV scattering bicone (see [Hines et al. 1999](#), for discussion), while the solid red lines show the  $1\sigma$  limits of the bicone opening angle.

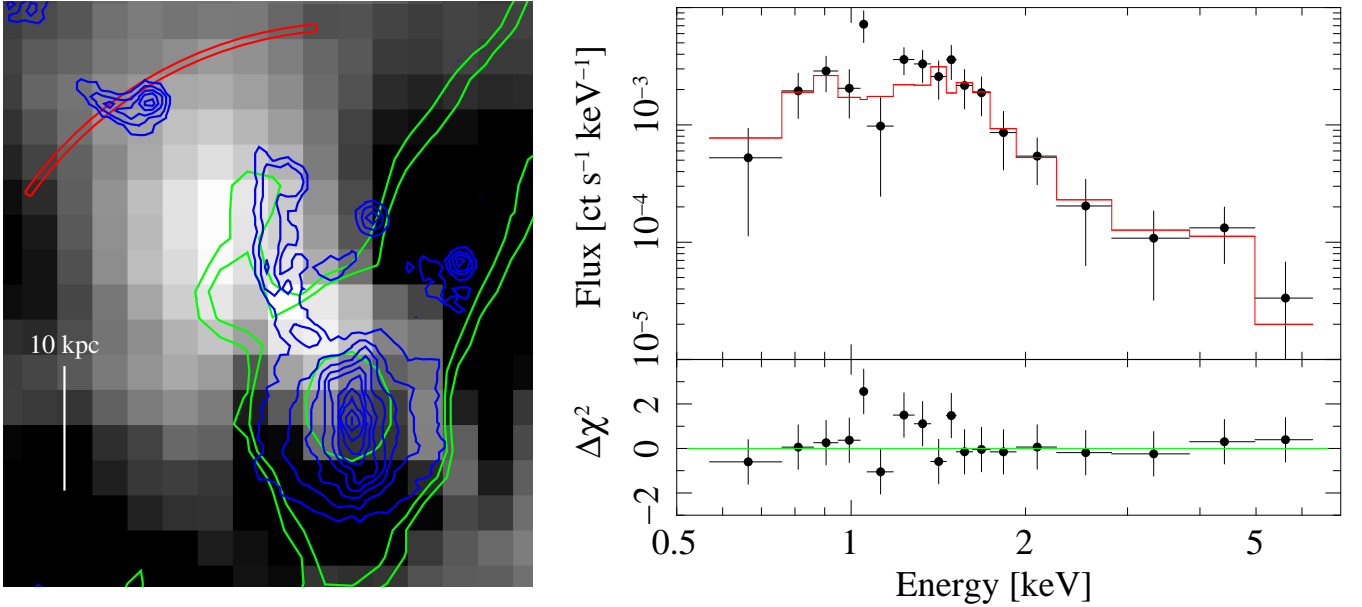


**Figure 5.** *Left:* Zoom-in of EEx overlaid with radio (green) and optical (blue) contours. Red wedge marks the extent of scattered UV emission. *Right:* Background-subtracted EEx spectrum binned to  $3\sigma$  significance. The red line is the best-fit CLOUDY model for a QSO irradiated nebula and ICM.

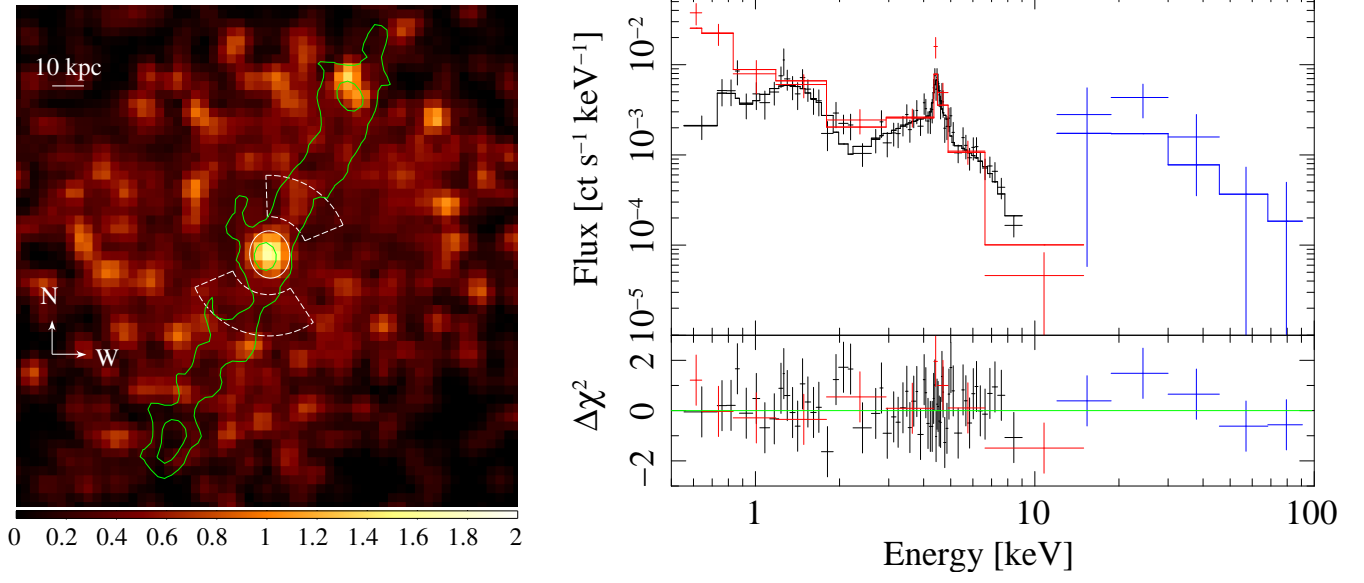


**Figure 6.** *Left:* X-ray HR map of the RX J0913.7+4056 core. Green contours trace the highest and lowest significance 1.4 GHz emission regions. White ellipse is the 90% EEf source region and dashed white wedges are background regions. The areas with the largest HR are coincident with the central source and the termination point of the northern radio jet. *Right:* Background-subtracted nuclear spectrum and best-fit model for the 1999 (red) & 2009 (black) *Chandra* data and 1998 *BeppoSAX* PDS data (blue). Data has been binned to  $3\sigma$  significance.